Electronic Supplementary Material (ESI) for Energy & Environmental Science.
This journal is © The Royal Society of Chemistry 2020

1. Supplementary Note: Calculation Details and Simplification/Assumption

Supplementary Note 1: General calculation details for the adsorption energies

Reaction energetics were calculated with density functional theory (DFT) with a periodic plane-wave implementation and ultrasoft pseudopotentials using the QUANTUM ESPRESSO code,[1] interfaced with the Atomistic Simulation Environment (ASE).[2] We applied the BEEF-vdW functional, which provides a reasonable description of van der Waals forces while maintaining an accurate prediction of chemisorption energies.[3] Plane-wave and density cutoffs were 500 and 5000 eV, respectively, with a Fermi-level smearing width of 0.1 eV. psLib ultrasoft pseudopotentials were chosen. The adsorption energies on (111) and (100) surfaces of *fcc* transition metals were evaluated using four-layer (3 × 3) supercells with the bottom two layers constrained and a vacuum layer of 20 Å, and [4 × 4 × 1] Monkhorst-Pack *k*-point grids[4] were used. The simulation of (211) surfaces of *fcc* transiton metals followed the same calculation settings but on four-layer (1 × 3) supercells. (3 × 1) supercells were also used to model Cu(310) and Cu(511) and Monkhorst-Pack *k*-point grids are [3 × 6 × 1] and [4 × 4 × 1], respectively.

All the cell sizes and corresponding Monkhorst-Pack *k*-point grids for other Cu facets and intermetallic surfaces could be found in **Table S1**.

Table S1. Computational details for materials and surfaces shown in the (G_{CO*}, G_{C*}) selectivity maps.

Materials	Surfaces	Unit cell size	Monkhorst-Pack k-point grids
Various Cu	(110)	(2 × 3)	[4 × 4 × 1]
	(711)	(3 × 1)	[4 × 3 × 1]
	(521)	(2 × 1)	[4 × 4 × 1]
	(621)	(2 × 1)	[3 × 4 × 1]
	(653)	(1 × 1)	[4 × 3 × 1]
	(111)-SV (1/9 single vacancy in the top layer)	(3 × 3)	[4 × 4 × 1]
$L1_2$ intermetallics	A_3B (100) with AB surface termination	(2√2 × 2√2)	[4 × 4 × 1]
$L1_0$ intermetallics	AB (100) with AB surface termination	(2√2 × 2√2)	[4 × 4 × 1]
Ni-Ga	Ni_3Ga (100)	(3√2 × 3√2)	[4 × 4 × 1]
	Ni_5Ga_3 (100)	(2√2 × 2√2)	[4 × 4 × 1]
	Ni_5Ga_3 (221)	(1 × 1)	[4 × 4 × 1]
	Ni_5Ga_3 (111)	(2 × 1)	[4 × 4 × 1]

All the surfaces have four layers with the top two layers relaxed. (100) surface orientations were selected due to the uniqueness of four-fold hollow site in stabilizing the C* intermediate compared to corresponding three-fold hollow site. The AB-type surface terminations for $L1_2$ and $L1_0$ intermetallics were selected due to the relatively low surface energy as shown in **Figure S1**.

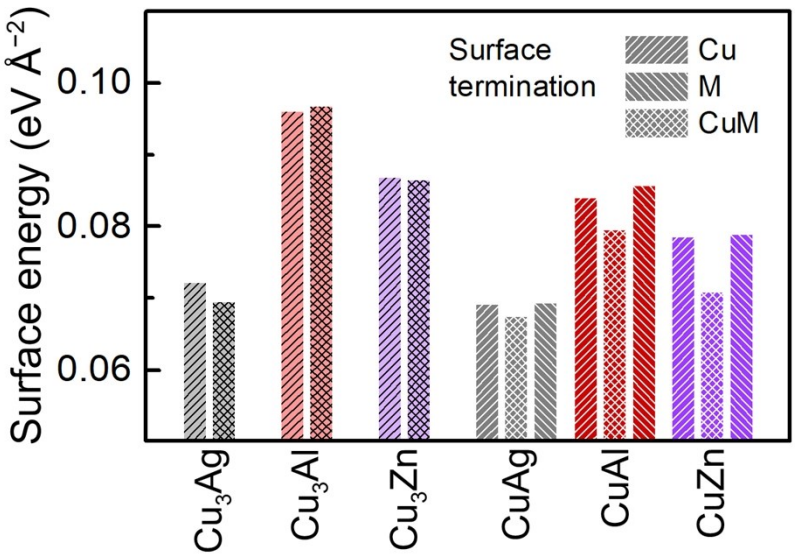

Figure S1. Surface energies of Cu-based intermetallics.

For a given slab exposed at the (hkl) plane with n atoms, its surface energy γ is given by $\gamma^{hkl} = (E^{hkl}_{slab} - E_{bulk}n_{slab})/(2A^{hkl}_{slab})$ where A^{hkl}_{slab} is the cross-sectional area of the slab's unit cell, n_{slab} the number of atoms in the slab, E^{hkl}_{slab} the energy of the slab itself, and E_{bulk} the energy of the optimized bulk structure per atom. Pure Cu and half Cu half M (CuM) surface terminations were considered for $L1_2$ A_3B intermetallics while pure Cu, pure M and CuM surface terminations were considered for $L1_0$ A_3B intermetallics. The Ni-rich surface terminations were selected for Ni-Ga systems based on the previous works considering both the surface energy and the CO adsorption.[5, 6]

All structures were optimized until the force components were less than 0.05 eV Å^{-1}. A dipole correction was applied to decouple the electrostatic interaction between the periodically repeated slabs.

Supplementary Note 2: Gibbs free energy correction

To directly obtain the reaction energies ΔG_{rxn} from energetic scaling relationship and use them for the selectivity maps, we used adsorption free energies, G, instead of electronic energies to construct those scaling relationships. Thus, G is affected by the selected gas-phase free energies as the references. Here we made the same assumption as Peterson et al. did in 2010[7] that gaseous products in the pathway were calculated at partial pressures corresponding to the Faradaic yields reported by Hori et al.[8] The fugacities we used are the same as in Ref.[7]. Therefore, the contribution to the chemical potential μ of gas-phase molecules could be found in **Table S2**.

Table S2. Gas-phase free energy correction. Assumed fugacity for each non-adsorbate species, along with calculated electronic energies (E_{raw}), DFT correction ($E_{BEEF\text{-}vdW}$), corrected electronic energies ($E_{ele} = E_{raw} + E_{BEEF\text{-}vdW}$), zero point energies (ZPE), enthalpic temperature correction, entropy contribution ($-TS$), chemical potential ($\mu = E_{ele} + \text{ZPE} + \int C_p dT - TS$), and the total correction ($\mu - E_{ele} = \text{ZPE} + \int C_p dT - TS$). H_2 is the value used for gaseous hydrogen, H_2 (ref) is used for the computational hydrogen electrode.

Species	Fugacity (Pa)	E_{raw} (eV)	$E_{BEEF\text{-}vdW}$ (eV)	E_{ele} (eV)	ZPE (eV)	$\int C_p dT$ (eV)	$-TS$ (eV)	μ (eV)	$\mu - E_{ele}$ (eV)
CO	5562	0.00		0.00	0.13	0.09	−0.67	−0.45	−0.45
H_2	30296	−0.09	0.09	0.00	0.27	0.09	−0.44	−0.07	−0.07
CH_4	20467	−2.80		−2.80	1.20	0.11	−0.67	−2.16	0.64
C_2H_4	13942	−3.14		−3.14	1.37	0.12	−0.74	−2.39	0.75
H_2O	3534	0.00		0.00	0.57	0.10	−0.67	0.00	0.00
H_2 (ref)	101325	−0.09	0.09	0.00	0.27	0.09	−0.41	−0.04	−0.04

E_{ele} and μ are referenced to the gas-phase electronic energy of CO, H_2O, and H_2 (ref) and μ is different from the free energy change (G, referenced to the gas-phase free energy) shown in **Figure 6**, **Figures S18–S22**, and **Table S9**. For example, $\mu_{CH4} = E_{ele\_CH4} + (\text{ZPE} + \int C_p dT - TS)_{CH4}$ while $G_{CH4} = \mu_{CH4} - (\mu_{CO} + 2 \times \mu_{H2\ (ref)} - \mu_{H2O})$.

Similarly, the free energy correction to the adsorbates could be found in **Table S3**. Modes of vibration were found by performing a normal-mode analysis; all vibrations were treated in the harmonic oscillator approximation. All vibrations used for free energy correction were obtained on Cu.

Table S3. Adsorbate free energy correction. Contributions to the adsorbate free energy from the ZPE correction, enthalpic temperature correction, entropy, and the total free energy correction, respectively.

Adsorbates	ZPE (eV)	$\int C_p dT$ (eV)	$-TS$ (eV)	$\mu - E_{ele}$ (eV)
CO*	0.17	0.07	−0.16	0.09
CHO*	0.44	0.09	−0.22	0.32
COH*	0.46	0.09	−0.17	0.37
C*	0.09	0.02	−0.03	0.08
CHOH*	0.76	0.09	−0.18	0.68
CH*	0.34	0.03	−0.05	0.33
CH_2*	0.59	0.06	−0.10	0.55
CH_3*	0.91	0.08	−0.15	0.84
OCCO*	0.42	0.10	−0.18	0.35
OCCOH*	0.72	0.11	−0.19	0.65
OCCHO*	0.64	0.09	−0.16	0.57
CCO*	0.33	0.09	−0.15	0.27
CHCO*	0.60	0.09	−0.22	0.47
H*	0.13	0.01	−0.02	0.12

OH*	0.32	0.07	−0.15	0.24

The ZPE shown in **Table S3** is only for Cu(100). Considering that G_{CO*} is one of the two descriptors, the ZPE used for correcting the CO adsorption free energies on various metals and different sites was replaced by the corresponding value shown in **Table S8 (see details in CO overbinding corrections)**.

Supplementary Note 3: Solvation correction

According to previous analysis,[9, 10] the solvation corrections ($E_{solv\ corr}$) to CO*, CHO*, COH*, CHOH*, OCCO*, OCCOH*, OCCHO*, CCO*, and CHCO* are summarized in **Table S4**. The binding energy after solvation correction $\Delta E_{solv} = \Delta E_{vacuum} - E_{solv\ corr}$, where ΔE_{vacuum} is the adsorption energy calculated without explicit solvents (in vacuum), $E_{solv\ corr}$ is the energetic correction listed in **Table S4**, and ΔE_{solv} is the solvation-corrected adsorption energy used in this work. The solvation correction for CHOH* is assumed to be the same as COH*; the solvation correction for OCCOH* is estimated from the that for OCCO* and the difference between CO* and COH*.

Table S4. Solvation corrections.

Adsorbates	$E_{solv\ corr}$ (eV)	Adsorbates	$E_{solv\ corr}$ (eV)
CO*[10]	−0.06	OCCO*[10]	−0.25
CHO*[10]	−0.11	OCCOH*	−0.30
COH*[10]	−0.11	OCCHO*[10]	−0.30
C*	0	CCO*[9]	−0.10
CHOH*	−0.11	CHCO*[9]	−0.10
CH*	0	H*	0
CH_2*	0	OH*	0
CH_3*	0	CO_{HP}	0

HP: Helmholtz plane;

Supplementary Note 4: Interface electric field model and field correction

Cation-induced fields lead to dramatic stabilizations of the C_2 species involved.[11] The more degrees of freedom in the solvent in the presence of cations and solvent rearrangement in the presence of bulkier C_2 intermediates, however, leads to higher uncertainties in the energetics. It has been suggested previously that the stabilization brought by solvation and cation-induced fields can roughly be divided,[11] and therefore we consider those two effects separately. We firstly obtained the field-stabilized adsorbate structures in the presence of a hydronium (H_3O^+) ion. We then applied a sawtooth potential in the *z*-direction for structures of the adsorbates in vacuum, where the solvent layer was removed. The interaction energy between the adsorbate and the interfacial field can be described by

$$\Delta\Delta E = \mu\varepsilon - \frac{1}{2}\alpha\varepsilon^2 + \ldots \quad (1)$$

where $\Delta\Delta E$ is the change in binding energy ΔE, ε is the electric field strength, and μ and α are the intrinsic dipole moment and polarizability of the adsorbate, respectively.[12] The

parameters μ and α of the key intermediates are shown in **Table S5**. Note that μ and α of OCCHO* and OC-CHO^{TS} are adopted from the data shown in Ref.[13] to justify the contribution of OC-CHO coupling to C_{2+} formation.

Table S5. Parameters that describe the field effect on adsorption energies.

Species	CO_{HP}	CO*	COH*	C*	CH*	
μ (eÅ)	0.0357	0.0440	−0.125	0.135	−0.00870	
α (eÅ^2 V^{-1})	0.254	0.302	0.514	−0.0752	0.0340	
Species	OCCO*	OCCOH*	TS: C-CO	CCO*	OCCHO*[13]	TS: OC-CHO[13]
μ (eÅ)	0.672	0.239	0.225	0.421	1.038	0.759
α (eÅ^2 V^{-1})	0.466	0.652	0.612	0.451	0.423	0.295

Note: CO_{HP}: CO in the Helmholtz plane; CH* is insensitive to the field and thus not considered for the field correction.

The field dependence of key intermediates is shown in **Figure S2a, b** using the above parameters of μ and α and Eq. (1).

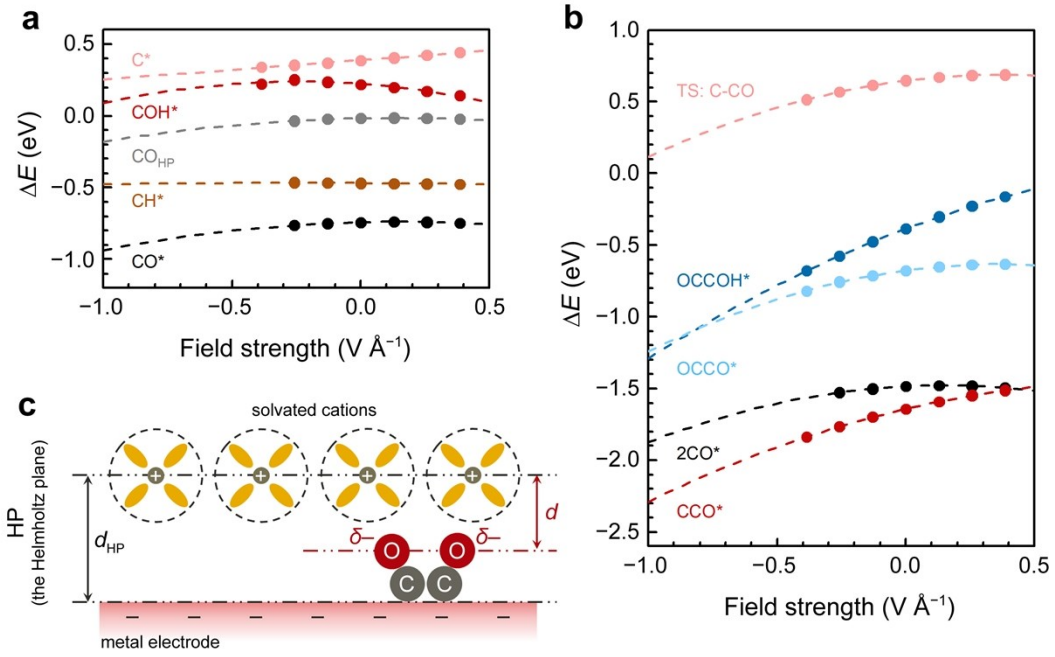

Figure S2. Field effect on energetics of key intermediates. Electronic adsorption energies of key (**a**) C_1 and (**b**) C_2 intermediates under various field strengths. These energies were corrected after solvation correction. All energetics were obtained on a (3×3×4) Cu(100) slab. (**c**) Schematic illustration of decreased d with respect to the usual thickness of the Helmholtz plane (d_{HP}) when negative charge is transferred to surface-bound key intermediates such as the $O^{\delta-}CCO^{\delta-}$ dimer. By applying the estimated d of 1.2 Å, the simple double layer capacitor model results in comparable adsorption energies of key species to those obtained with a more sophisticated model recently developed by Chan et al..[14]

Then, it is important to correlate the interfacial electric field strength to the applied potential for the Cu(100) electrode. According to the classical double layer theory,[15] the electric field strength ε is derived from

$$\varepsilon = \frac{\Phi_M - \Phi_{M,\,PZC}}{d} \quad (2)$$

where Φ_M and $\Phi_{M,\,PZC}$ are applied potential of a metal electrode and the zero-charge potential of this metal electrode, respectively, and d is the distance between the positively (*i.e.* the center of the Helmholtz plane) and negatively charged planes. $\Phi_{M,\,PZC}$ approximates the electrolyte potential at the Helmholtz plane (Φ_{HP}), and the potential difference $\Phi_M - \Phi_{HP}$ is defined as the driving force for the interfacial charge transfer that builds the electric field.[16] Eq. (2) explicitly introduces the potential dependence of ε. Herein experimentally measured $\Phi_{M,\,PZC} = -0.54$ V vs. the standard hydrogen electrode (SHE) for Cu(100)[14, 17] and $d = 1.2$ Å were employed in our simulation. Note that $d = 1.2$ Å is smaller than the usually simulated thickness (ca. 3–4 Å) of the Helmholtz plane.[14, 18] **Figure S2c** depicts the decreased d with negative charge transferred to surface-bound key intermediates such as the $O^{\delta-}CCO^{\delta-}$ dimer.

Despite the above estimation of d, our model shows reasonable agreement of the binding energy of OCCO* on Cu(100) at –1.0 V vs. RHE (pH = 7) with the value reported by Chan et al. employing a combined multiscale *ab initio*/continuum model that describes the effect of surface charge density σ and electric field more strictly (**Figure S3**).[14]

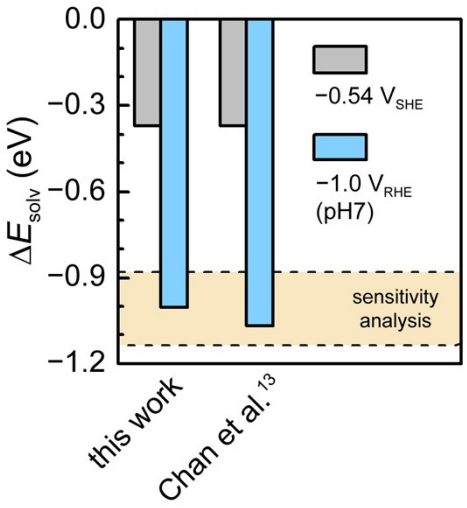

Figure S3. Comparison between OCCO* adsorption energies on Cu(100) using different methods. OCCO* is regarded as the most important intermediate in the OCCOH pathway and is very sensitive to field. The OCCO* adsorption energies used in this work, derived through the field model described by Eq. (1), are compared to the reported values by Chan et al. using a multiscale *ab initio*/continuum model using surface charge density σ as a descriptor.[14]

As reported in Ref.[14], the OCCO* adsorption energies on Cu(100) are given as $\Delta E = -0.37 + 0.0393\sigma - 0.00025\sigma^2$ and σ was estimated to be −18 μC cm^{-2} at $U_{RHE} = -1.0$ V in a K^+-based neutral electrolyte (*i.e.*, the similar system as the experimentally tested $KHCO_3$ electrolyte at pH = 6.8 and the pH = 7 microkinetic model in this work). The

comparison shows reasonable agreement in the OCCO* adsorption energies between our simplified field model and higher-level σ-based simulations within the range of DFT error.[14, 19] Sensitivity analysis was performed by varying d from 1.0 to 1.4 Å and the induced difference in binding energies is also within the range of DFT error. Similar sensitivity analysis was also performed in **Figure S10**. Thus we believe that our treatment of the field effect will not induce strong deviation from the results obtained through higher-level σ-based simulations.

With including the above U_{SHE}-dependent field effect and the computational hydrogen electrode (CHE) model[20] that brings in energetic correction to electrons at a U_{RHE} scale, the electronic adsorption energy of a certain specie at a given $U_{SHE/RHE}$ is given by

$$\Delta E_{ads}^{U_{SHE/RHE}} = \Delta E_{ads}^{U_{RHE}=0} + neU_{RHE} + \frac{\mu}{d}(U_{SHE} - U_{M,PZC}) - \frac{1}{2}\frac{\alpha}{d^2}(U_{SHE} - U_{M,PZC})^2 \quad (3)$$

(U_{RHE} scale) (U_{SHE} scale)

where $\Delta E_{ads}^{U_{RHE}=0}$ is the adsorption energy at U_{RHE} = 0 V (referenced to gas-phase CO, H_2O, and H_2), n is the number of transferred electron, $U_{M,PZC}$ = –0.54 V vs. SHE for Cu(100), while U_{SHE} and U_{RHE} are correlated through the pH of the bulk electrolyte

$$U_{RHE} = U_{SHE} + 0.059\text{pH} \quad (4)$$

Note that the U_{SHE}-scale term in Eq. (3) is only applied to field-sensitive species as shown in **Figure S3** and other species follow the U_{RHE}-scale dependency. Lastly, we added the solvation corrections as described above to obtain the adsorption energies. The obtained adsorption energies used for microkinetic modeling are shown in **Table S6**.

Table S6. Electronic energies $E_{ads}^{U_{RHE}=0}$ and chemical potentials $\mu_{ads}^{U_{RHE}=0}$ of species involved in the microkinetic modeling on Cu(100).

Conditions	vacuum	solv		field correction applied?
Adsorbates	$E_{ads}^{U_{RHE}=0}$ (eV)	$E_{ads}^{U_{RHE}=0}$ (eV)	$\mu_{ads}^{U_{RHE}=0}$ (eV)	(*yes* or *no*)
CO*	−0.65	−0.71	−0.62	*yes*
CHO*	0.01	−0.10	0.22	*no*
COH*	0.34	0.23	0.60	*yes*
C*	0.38	0.38	0.46	*yes*
CHOH*	0.03	−0.08	0.60	*no*
CH*	−0.47	−0.47	−0.14	*no*
CH_2*	−0.60	−0.60	−0.05	*no*
CH_3*	−1.68	−1.68	−0.84	*no*
OCCO*	−0.12	−0.37	−0.02	*yes*
OCCOH*	−0.38	−0.68	−0.03	*yes*
OCCHO*	−0.06	−0.36	0.21	*yes*
CCO*	−1.62	−1.72	−1.45	*yes*
CHCO*	−1.75	−1.85	−1.38	*no*
H*	0.07	0.07	0.19	*no*

OH*	−0.04	−0.04	0.20	*no*
CO_{HP}	0.00	0.00	−0.45	*yes*

Note: CO_{HP}: CO in the Helmholtz plane

Ongoing efforts will evaluate the energetics more rigorously by minima hopping[11, 21] the cation/solvent structures in the presence of the various intermediates. This method has been well adopted in previous works.[9, 13, 22, 23]

Supplementary Note 5: Electrochemical barriers and hydronium vs. water as the hydrogen source for proton transfer

Electrochemical barriers were calculated with (3 × 3) and (4 × 3) supercells and Monkhorst-Pack k-point grids of [4 × 4 × 1] and [3 × 4 × 1], respectively. All structures contained a three-layer transition metal slab, with atoms in the top layer relaxed and the rest fixed, along with a hydrogen-bonded water layer determined through minima hopping.[11] Transition state (TS) geometries and energies were calculated using the climbing-image nudged elastic band (CI-NEB) method, with the forces on the climbing image converged to less than 0.05 eV $Å^{-1}$.[24] The spring constants were tightened for images close to the saddle point.[25] The plane wave and charge density cutoff, exchange-correlation functional, and other parameters were the same as those used for geometry optimizations. The charge extrapolation method[26, 27] was used to deduce the activation barriers at constant potential.[28] A H_3O^+ ion was present in the initial state (IS) to act as the hydrogen source for protonation. Later on, we will introduc an approach to estimate alkaline protonation barriers (water as the hydrogen source) from the barriers obtained under acidic conditions (H_3O^+).

We note that all of the reported barriers are acidic barriers, *i.e.*, H_3O^+ as the hydrogen source. However, at neutral and alkaline conditions, the concentration of H_3O^+ is lower than 10^{-7} M in the aqueous solution at room temperature. Recent experimental and theoretical works also showed that water should be the dominant hydrogen source for protonation at neutral and alkaline conditions.[29, 30] The difficulties in obtaining alkaline electrochemical barriers through DFT computation have been discussed in details in previous works.[9, 30] Taking these difficulties into consideration, we therefore estimated alkaline barriers from the acidic ones based on the following analysis regarding pH effects on the IS/FS energies and the choice of potential scales of RHE/SHE.

According to previous studies of a protonation reaction,[9, 31] the pH affects the chemical potential of OH^- and H_3O^+ through their configurational entropies, while the absolute potential (i.e. U_{SHE}) affects the chemical potential of the electron, e^-. As the TS is assumed to have no entropic contributions, its energy only depends on potential via the fractional and pH-independent transfer coefficient α. In the case of H_3O^+ as the hydrogen source,

$$X^* + H_3O^+ + e^- \rightarrow XH^* + H_2O \quad (5)$$

the activation energy and the reaction energy can be expressed as

$$\Delta G_{a}^{H_3O^+} = \mu_{TS} + \mu_{\alpha e^-, U} - \left(\mu_{H_3O^+} + \mu_{e^-, U} + \mu_{X^*}\right)$$

$$= \mu_{TS} + (\mu_{\alpha e^-,0} - \alpha e U_{SHE}) - \left((\mu^{0}_{H_3O^+} - 2.3k_B T\text{pH}) + \left(\mu_{e^-,0} - eU_{SHE}\right) + \mu_{X*}\right)$$

$$= \Delta G^{H_3O^+}_{a,0} + \beta e U_{SHE} + 2.3k_B T\text{pH} \quad (6)$$

$$= \Delta G^{H_3O^+}_{a,0} + \beta e U_{RHE} + (1-\beta)2.3k_B T\text{pH} \quad (7)$$

$$\Delta G^{H_3O^+} = \mu_{XH*} + \mu_{H_2O} - \left(\mu_{H_3O^+} + \mu_{e^-,U} + \mu_{X*}\right)$$

$$= \mu_{XH*} + \mu_{H_2O} + \left((\mu^{0}_{H_3O^+} - 2.3k_B T\text{pH}) + \left(\mu_{e^-,0} - eU_{SHE}\right) + \mu_{X*}\right)$$

$$= \Delta G^{H_3O^+}_{0} + eU_{SHE} + 2.3k_B T\text{pH} \quad (8)$$

$$= \Delta G^{H_3O^+}_{0} + eU_{RHE} \quad (9)$$

In the case of water as the hydrogen source,

$$X^* + H_2O + e^- \rightarrow XH^* + OH^- \quad (10)$$

the activation energy and the reaction energy can be expressed as

$$\Delta G^{H_2O}_{a} = \mu_{TS} + \mu_{\alpha e^-,U} - \left(\mu_{H_2O} + \mu_{e^-,U} + \mu_{X*}\right)$$

$$= \mu_{TS} + (\mu_{\alpha e^-,0} - \alpha e U_{SHE}) - \left(\mu_{H_2O} + \left(\mu_{e^-,0} - eU_{SHE}\right) + \mu_{X*}\right)$$

$$= \Delta G^{H_2O}_{a,0} + \beta e U_{SHE} \quad (11)$$

$$= \Delta G^{H_2O}_{a,0} + \beta e U_{RHE} - \beta 2.3k_B T\text{pH} \quad (12)$$

$$\Delta G^{H_2O} = \mu_{XH*} + \mu_{OH^-} - \left(\mu_{H_2O} + \mu_{e^-,U} + \mu_{X*}\right)$$

$$= \mu_{XH*} + (\mu^{0}_{OH^-} - 2.3k_B T(14 - \text{pH})) - \left(\mu_{H_2O} + \left(\mu_{e^-,0} - eU_{SHE}\right) + \mu_{X*}\right)$$

$$= \Delta G^{H_2O}_{0} + eU_{SHE} + 2.3k_B T\text{pH} \quad (13)$$

$$= \Delta G^{H_2O}_{0} + eU_{RHE} \quad (14)$$

where $\mu^{0}_{OH^-}$ and $\mu^{0}_{H_3O^+}$ denote the chemical potentials under the standard conditions, μ_{X*} and μ_{XH*} the chemical potential of species X* and XH*, $\Delta G^{H_2O}_{a,0}$ / $\Delta G^{H_2O}_{0}$ the activation energy and reaction energy at 0 V using water as the hydrogen source, $\Delta G^{H_3O^+}_{a}$ / $\Delta G^{H_3O^+}_{0}$ the activation energy and reaction energy at 0 V using H_3O^+ as the hydrogen source, α the charge in the TS that gives the potential dependence ($\beta = 1 - \alpha$), T the temperature and k_B the Boltzmann constant.

According to the equations above, the activation energies and reaction energies of acidic and alkaline protonation reactions can be schematically illustrated as in **Figure S4** at different potential scales. Eq. (6) and Eq. (11) show that the acidic barrier is dependent on

both pH and absolute potential while the alkaline barrier only depends on the absolute potential; Eq. (9) and Eq. (14) express that the reaction energies of both acidic and alkaline protonation reactions are U_{RHE}-dependent. On the SHE scale, an increased pH leads to an increased acidic barrier by an amount of $2.3k_BT\Delta pH$, while the alkaline barrier is unaffected by pH. While in RHE scale, since shifts in pH are by definition balanced by shifts in absolute potential (i.e. $2.3k_BT\Delta pH = -e\Delta U$), an increased pH will lead to an increase in acidic barriers by an amount of $(1-\beta)2.3k_BT\Delta pH$ and a decrease in barriers from water by an amount of $\beta 2.3k_BT\Delta pH$.

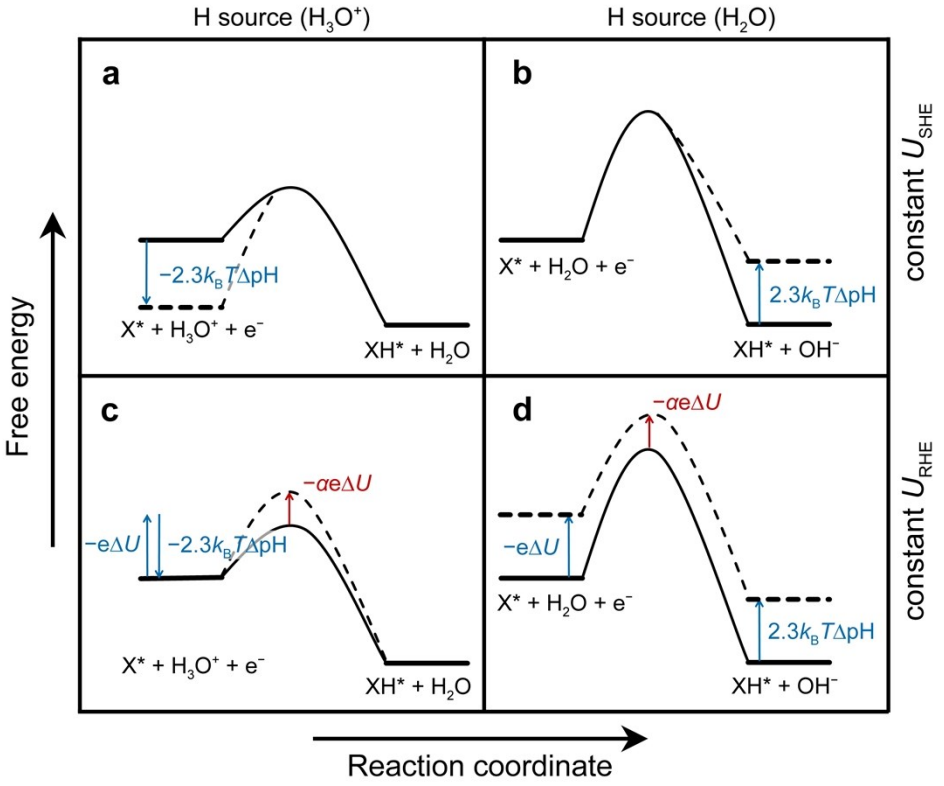

Figure S4. The effects of H_3O^+ and H_2O as hydrogen sources on activation/reaction energies of a protonation reaction. Free energy profiles of (**a**) acidic protonation with H_3O^+ as the hydrogen source and (**b**) alkaline protonation with H_2O as the hydrogen source at a constant absolute potential of U_{SHE}. Free energy profiles of (**c**) acidic protonation with H_3O^+ as the hydrogen source and (**d**) alkaline protonation with H_2O as the hydrogen source at the same potential of U_{RHE}. pH increases from solid profile to dashed profile in each panel. The schematic illustration was conceptualized for the Volmer reaction in Ref.[31].

To correlate the acidic and alkaline barriers using different hydrogen sources, we firstly extrapolated the barriers to a work function of 4.4 eV, which corresponds to 0 V vs. SHE. All TSs were referenced to the IS of aqueous protons and electrons in bulk solution, as determined using the CHE.[20]

According to previous study by Liu et al.,[9] there is an energetic difference between the acidic barrier at 0 V vs. RHE at pH = 0 ($\Delta G_{a,\,0\,V_{RHE},\,pH0}^{H_3O^+}$, also equivalent to $\Delta G_{a,\,0\,V_{SHE},\,pH0}^{H_3O^+}$) and

the alkaline barrier at 0 V vs. RHE at pH = 14 ($\Delta G_{\mathrm{a,\,0\,V_{RHE},\,pH14}}^{\mathrm{H_2O}}$) for the Volmer and Heyrovsky reactions (Supplementary Table 3 in Ref.[9]). We therefore refer such an energetic difference as "alkaline barrier correction" as determined by

$$\Delta\Delta G_{\mathrm{alkaline\ corr}} = \Delta G_{\mathrm{a,\,0\,V_{RHE},\,pH14}}^{\mathrm{H_2O}} - \Delta G_{\mathrm{a,\,0\,V_{RHE},\,pH0}}^{\mathrm{H_3O^+}} \quad (15)$$

According to Eq. (6), Eq. (10), and Eq. (15), we could then correlate the alkaline barrier at 0 V vs. RHE at pH = 7 ($\Delta G_{\mathrm{a,\,0\,V_{RHE},\,pH7}}^{\mathrm{H_2O}}$) to the acidic barrier at 0 V vs. SHE at pH = 7 ($\Delta G_{\mathrm{a,\,0\,V_{SHE},\,pH7}}^{\mathrm{H_3O^+}}$) through:

$$\begin{aligned}\Delta G_{\mathrm{a,\,0\,V_{RHE},\,pH7}}^{\mathrm{H_2O}} &= \Delta G_{\mathrm{a,\,0\,V_{RHE},\,pH14}}^{\mathrm{H_2O}} - \beta 2.3 k_{\mathrm{B}} T(7-14) \\ &= (\Delta G_{\mathrm{a,\,0\,V_{RHE},\,pH0}}^{\mathrm{H_3O^+}} + \Delta\Delta G_{\mathrm{alkaline\ corr}}) - \beta 2.3 k_{\mathrm{B}} T(7-14) \\ &= ((\Delta G_{\mathrm{a,\,0\,V_{SHE},\,pH7}}^{\mathrm{H_3O^+}} - 2.3 k_{\mathrm{B}} T(7-0)) + \Delta\Delta G_{\mathrm{alkaline\ corr}}) - \\ &\quad \beta 2.3 k_{\mathrm{B}} T(7-14) \\ &= \Delta G_{\mathrm{a,\,0\,V_{SHE},\,pH7}}^{\mathrm{H_3O^+}} + \Delta\Delta G_{\mathrm{alkaline\ corr}} - (1-\beta) 2.3 k_{\mathrm{B}} T \times 7\end{aligned} \quad (16)$$

The charge transfer coefficient β is determined explicitly from the Bader charge analysis. However, determining the exact $\Delta\Delta G_{\mathrm{alkaline\ corr}}$ for each single protonation step will be tedious and computational challenging as we discussed above (see Page 8). Therefore, we assume that the effect of altering hydrogen source from H_3O^+ to water on other protonation reactions is the same as on the Volmer reaction. If we assume a protonation reaction with $\beta = 0.5$ and $\Delta\Delta G_{\mathrm{alkaline\ corr}} = 0.21$ eV, the alkaline barrier $\Delta G_{\mathrm{a,\,0\,V_{RHE},\,pH7}}^{\mathrm{H_2O}}$ is estimated to have a similar height to the acidic barrier of $\Delta G_{\mathrm{a,\,0\,V_{SHE},\,pH7}}^{\mathrm{H_3O^+}}$ based on Eq. (16): both would be 0.42 eV higher than $\Delta G_{\mathrm{a,\,0\,V_{RHE},\,pH0}}^{\mathrm{H_3O^+}}$.

We note that our assumption for $\Delta\Delta G_{\mathrm{alkaline\ corr}}$ is entirely based on a comparison from previously calculated barriers for the hydrogen evolution reaction (HER),[9] and that changes in β and $\Delta\Delta G_{\mathrm{alkaline\ corr}}$ will result in barrier differences between $\Delta G_{\mathrm{a,\,0\,V_{RHE},\,pH7}}^{\mathrm{H_2O}}$ and $\Delta G_{\mathrm{a,\,0\,V_{SHE},\,pH7}}^{\mathrm{H_3O^+}}$. H_3O^+ is inherently less stable than water at standard conditions, and thus the energetic difference between the alkaline barriers relative to the acidic barriers is expected to be positive. Next, it has been experimentally measured in Markovic's group that the exchange current density of HER is two to three orders of magnitude lower when operating under alkaline conditions (0.1 M NaOH, pH = 13)[32] compared to acidic conditions (0.1 M $HClO_4$, pH = 1)[33]. Thus, the experimentally determined activation energies are $\Delta H_{\mathrm{a,\,0\,V_{RHE},\,pH1}}^{\mathrm{H_3O^+}} = 0.19$ eV and $\Delta H_{\mathrm{a,\,0\,V_{RHE},\,pH13}}^{\mathrm{H_2O}} = 0.48$ eV, respectively. As the TS is assumed

to have no entropic contributions, the $\Delta G_{a,\,0\,V_{RHE},\,pH0}^{H_3O^+}$ and $\Delta G_{a,\,0\,V_{RHE},\,pH14}^{H_2O}$ could be determined as 0.21 eV and 0.44 eV based on Eq. (7) and Eq. (12), respectively, if a β of 0.65 (the same as in **Table S7**) is employed. Therefore, the $\Delta\Delta G_{\text{alkaline corr}}$ is determined as 0.23 eV using experimentally available data for HER. If we assume a worse-case alkaline barrier correction $\Delta\Delta G_{\text{alkaline corr}}$ = 0.25 eV, the largest change in $\Delta G_{a,\,0\,V_{RHE},\,pH7}^{H_2O}$ is found to be 0.085 eV for the Reaction 11 with a β of 0.6; and the smallest change is 0.023 eV for the Reaction 8 with a β of 0.45; while for the rest of protonation reactions with a β of 0.5, the change is 0.04 eV. These changes are well within DFT errors for determining barriers in general; therefore, we focus more on the trends rather than exact barrier values.

Table S7 lists the estimated $\Delta G_{a,\,0\,V_{RHE}}^{H_2O}$ for protonation steps within the $CO_{(2)}R$, using an alkaline correction of $\Delta\Delta G_{\text{alkaline corr}}$ = 0.21 eV. The barriers for the Volmer and Heyrovsky reactions (Reaction 1 and 2 in **Table S7**) were explicitly corrected using $\Delta\Delta G_{\text{alkaline corr}}$ = 0.25 eV and 0.37 eV, respectively, according to Ref.[9].

Table S7. Forward activation energies ΔG_a and backward activation energies ΔG_b at U_{RHE} = 0 V. The charge-transfer coefficient β for each protonation step is also provided. β was determined by calculating the Bader charge of TS. ΔG_b was used during charge extrapolation for obtaining the barriers of Reaction 8 and 10. These barriers remain unchanged in the microkinetic modeling at a certain pH.

Reaction index	Reaction	β	pH = 7		pH = 13	
			ΔG_a (eV)	ΔG_b (eV)	ΔG_a (eV)	ΔG_b (eV)
1	$H^+ + e^- + * \leftrightarrow H^*$	0.65	1.33		1.10	
2	$H^+ + e^- + H^* \leftrightarrow H_2(g) + *$	0.65	1.01		0.78	
3	$H^* + H^* \leftrightarrow H_2(g) + 2*$		0.92		0.92	
4	$CO^* + H^+ + e^- \leftrightarrow CHO^*$	0.50	1.36		1.18	
5	$CO^* + H^* \leftrightarrow CHO^* + *$		1.13		1.13	
6	$CO^* + H^+ + e^- \leftrightarrow COH^*$	0.50	1.10		0.92	
7	$CHO^* + H^+ + e^- \leftrightarrow CHOH^*$		0.18		0.18	
8	$COH^* + H^+ + e^- \leftrightarrow C^* + H_2O(g)$	0.45		0.80		0.61
9	$COH^* + H^* \leftrightarrow CHOH^* + *$		0.67		0.67	
10	$CHOH^* + H^+ + e^- \leftrightarrow CH^* + H_2O(g)$	0.50		1.73		1.55
11	$C^* + H^+ + e^- \leftrightarrow CH^*$	0.60	0.91		0.70	
12	$C^* + H^* \leftrightarrow CH^* + *$		0.58		0.58	
13	$CH^* + H^+ + e^- \leftrightarrow CH_2^*$	0.50	0.98		0.80	
14	$CH^* + H^* \leftrightarrow CH_2^* + *$		0.62		0.62	
15	$CH_2^* + H^+ + e^- \leftrightarrow CH_3^*$	0.50	0.80		0.62	
16	$CH_2^* + H^* \leftrightarrow CH_3^* + *$		0.62		0.62	
17	$CH_3^* + H^+ + e^- \leftrightarrow CH_4(g) + *$	0.50	0.72		0.54	
18	$CH_3^* + H^* \leftrightarrow CH_4(g) + 2*$		0.33		0.33	

19	$OCCO^{**} + H^+ + e^- \leftrightarrow OCCOH^{**}$	0.50	0.57	0.39
20	$CO^* + COH^* \leftrightarrow OCCOH^{**}$		0.87	0.87
21	$CO^* + CHO^* \leftrightarrow OCCHO^{**}$		1.05	1.05
22	$CO^* + C^* \leftrightarrow CCO^* + *$		0.73	0.73
23	$CO_{HP} + C^* \leftrightarrow CCO^*$		0.31	0.31
24	$CCO^* + H^+ + e^- \leftrightarrow CHCO^*$	0.50	0.87	0.69
25	$CO^* + CH^* \leftrightarrow CHCO^* + *$		0.97	0.97
26	$CH_2^* + CH_2^* \leftrightarrow C_2H_4(g) + 2^*$		0.69	0.69

* one surface site; ** two surface sites; HP: Helmholtz plane; TSs of the chemical coupling reactions including Reactions 21–23 are considered for the field effect described in **Supplementary Note 4**.

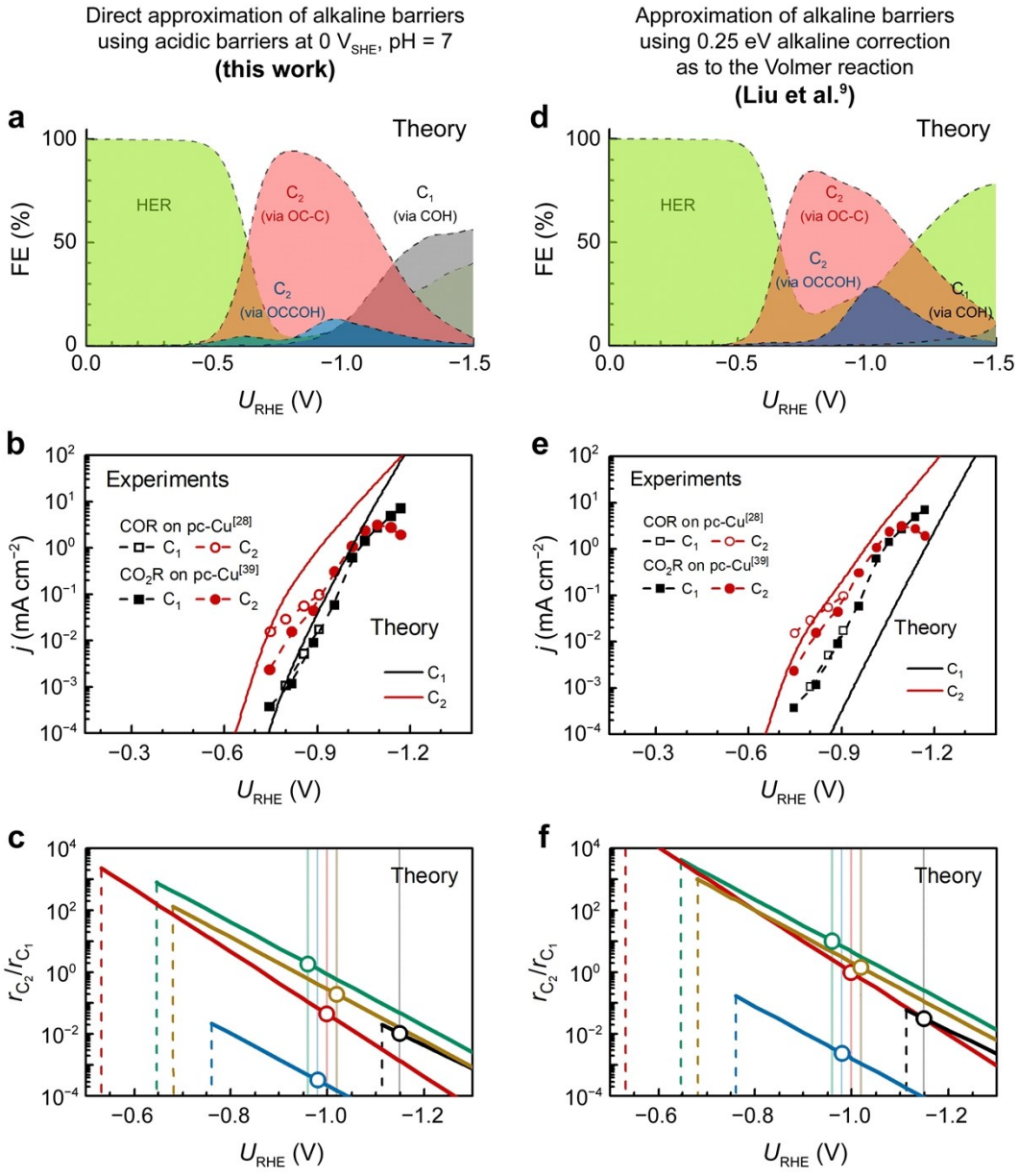

Figure S5. Comparison between two approaches of approximating the alkaline barriers from the acidic barriers. (Left) Direct approximation of $\Delta G_{a,\,0\ V_{RHE},\,pH7}^{H_2O}$ as $\Delta G_{a,\,0\ V_{SHE},\,pH7}^{H_3O^+}$: (**a**–**c**) microkinetic modeling results shown in this work as **Figure 3a**, **Figure 3b**, and **Figure 5d**, respectively. (Right) Approximation of $\Delta G_{a,\,0\ V_{RHE},\,pH7}^{H_2O}$ based on Eq. (16) using the same $\Delta\Delta G_{alkaline\ corr}$ = 0.25 eV as to the Volmer reaction and the explicit numbers of β: (**d**–**f**) modified microkinetic modeling results.

The comparison between microkinetic modeling results based on two approximation methods for alkaline barriers is shown in **Figure S5**. Compared to the results present in this work, the above changes due to approximative method for alkaline barriers, as well as in the activation energies of key steps including Reaction 6, 8, 11, and 19 in **Table S7**, induce some differences to the microkinetic modeling leading to dissimilar observations:

- The overall rate of COR through the COH/OC-C pathway is lowered due to the slight increase in CO-H barrier, leading to more predominant HER across the studied potential range.
- The relative dominance of the COH/OC-C pathway vs. the OCCOH pathway in reaction rates is weakened due to the slight increase in CO-H barrier vs. the unchanged CO dimerization reaction energy.
- The C_1 pathway through C-H protonation is suppressed due to the largest change in barrier vs. the unchanged C-CO coupling barrier, resulting in a more negative potential at which the C_1 rate equals to the C_2 rate.
- The predicted r_{C_2}/r_{C_1} becomes higher for every single-crystal Cu facets and quantitatively closer to the experimental values, but the general trends in C_2/C_1 selectivity among different Cu facets remain unchanged.

Overall, the trends described and the theoretical insights obtained in this work are consistent whether we use the $\Delta G_{a,\,0\ V_{SHE},\,pH7}^{H_3O^+}$ to directly estimate $\Delta G_{a,\,0\ V_{RHE},\,pH7}^{H_2O}$ or a $\Delta\Delta G_{alkaline\ corr}$ = 0.25 eV to correct the $\Delta G_{a,\,0\ V_{SHE},\,pH0}^{H_3O^+}$ to $\Delta G_{a,\,0\ V_{RHE},\,pH14}^{H_2O}$. Nevertheless, we point out that:

- Despite the higher barriers at the same U_{RHE}, water is more likely to be the hydrogen source for protonation reactions at neutral and alkaline conditions due to the abundance of water and the extremely low availability of H_3O^+ at these conditions.
- Any underestimation of the alkaline protonation barriers will result in overestimated rate of the reduction step vs. the C–C coupling step starting from the same surface species (*e.g.*, CO-H protonation vs. CO dimerization; C-H protonation vs. C-CO coupling)

Supplementary Note 6: Details of the microkinetic models

Mean-field microkinetic models are simulated with the CATMAP software package.[34] The CatMAP software package used in this work can be accessed and downloaded through https://github.com/SUNCAT-Center/catmap. In our microkinetic models, CH_4(g) was taken as an example of C_1 products, C_2H_4(g) was taken as an example of C_2 products, and

H_2(g) was included as the main side product. We note that as mentioned in the main text, we have assumed all the reaction steps after the formation of OCCH* to be downhill in energy. And therefore the results will remain unchanged whether the example C_2 product is chosen to be ethanol or ethylene. Both proton-electron transfer and surface hydrogenation pathways were taken into account. All the elementary steps are described as follows:

$H^+ + e^- + * \leftrightarrow$ H-ele* $\leftrightarrow$ H*

$H^+ + e^- + H^* \leftrightarrow H_2$-ele* $\leftrightarrow H_2(g) + *$

$H^* + H^* \leftrightarrow$ H-H* + * $\leftrightarrow H_2(g) + 2^*$

$OH^* + H^+ + e^- \leftrightarrow H_2O(g) + *$

$CO(g) \leftrightarrow CO_{HP}$

$CO_{HP} + * \leftrightarrow CO^*$

$CO^* + H^+ + e^- \leftrightarrow$ H-CO-ele* $\leftrightarrow$ CHO* (only applied for **Figures S7, S11**)

$CO^* + H^* \leftrightarrow$ H-CO* + * $\leftrightarrow$ CHO* + *

$CHO^* + H^+ + e^- \leftrightarrow$ CHO-H-ele* $\leftrightarrow$ CHOH*

$CO^* + H^+ + e^- \leftrightarrow$ CO-H-ele* $\leftrightarrow$ COH*

$COH^* + H^+ + e^- \leftrightarrow$ COH-H-ele* $\leftrightarrow C^* + H_2O(g)$

$COH^* + H^* \leftrightarrow$ COH-H* + * $\leftrightarrow$ CHOH* + *

$CHOH^* + H^+ + e^- \leftrightarrow$ CHOH-H-ele* $\leftrightarrow CH^* + H_2O(g)$

$C^* + H^+ + e^- \leftrightarrow$ C-H-ele* $\leftrightarrow$ CH*

$C^* + H^* \leftrightarrow$ C-H * + * $\leftrightarrow$ CH* + *

$CH^* + H^+ + e^- \leftrightarrow$ CH-H-ele* $\leftrightarrow CH_2^*$

$CH^* + H^* \leftrightarrow$ CH-H * + * $\leftrightarrow CH_2^* + *$

$CH_2^* + H^+ + e^- \leftrightarrow CH_2$-H-ele* $\leftrightarrow CH_3^*$

$CH_2^* + H^* \leftrightarrow CH_2$-H * + * $\leftrightarrow CH_3^* + *$

$CH_3^* + H^+ + e^- \leftrightarrow CH_3$-H-ele* $\leftrightarrow CH_4(g) + *$

$CH_3^* + H^* \leftrightarrow CH_3$-H * + * $\leftrightarrow CH_4(g) + 2^*$

$2CO^* \leftrightarrow$ OCCO**

$OCCO^{**} + H^+ + e^- \leftrightarrow$ OCCO-H-ele** $\leftrightarrow$ OCCOH**

$OCCOH^{**} + H^+ + e^- \leftrightarrow CCO^* + H_2O(g) + *$

$CO^* + C^* \leftrightarrow$ OC-C** $\leftrightarrow CCO^* + *$

$CO_{HP} + C^* \leftrightarrow$ C-CO* $\leftrightarrow$ CCO*

$CCO^* + H^+ + e^- \leftrightarrow$ OCC-H-ele* $\leftrightarrow$ CHCO*

$CO^* + CH^* \leftrightarrow$ OC-CH** $\leftrightarrow CHCO^* + *$

$CHCO^* + 5(H^+ + e^-) \leftrightarrow C_2H_4(g) + H_2O(g) + *$

$CH_2^* + CH_2^* \leftrightarrow CH_2$-$CH_2$** $\leftrightarrow C_2H_4(g) + 2^*$

$CO^* + COH^* \leftrightarrow$ OC-COH** $\leftrightarrow$ OCCOH** (only applied for **Figure S11**)

$CO^* + CHO^* \leftrightarrow$ OC-CHO** $\leftrightarrow$ OCCHO** (only applied for **Figure S11**)

$OCCHO^{**} + 7(H^+ + e^-) \leftrightarrow C_2H_4(g) + 2H_2O + 2^*$ (only applied for **Figure S11**)

(* one surface site; ** two surface sites; HP: Helmholtz plane)

Note that all above reactions actually use alkaline barriers of $\Delta G_{a,0\,V_{RHE}}^{H_2O}$ shown in **Table S7** and the alkaline protonation step of $X^* + H_2O + e^- \rightarrow XH^* + OH^-$ is written as the corresponding acidic form of $X^* + H^+ + e^- \rightarrow XH^*$ to fit with the CATMAP software package, in which the CHE model is implemented in to correct the energies of proton and

electron at a RHE scale.[20] And the actual concentration of H^+ is defined to be the same as water probability [H_2O] of 1.

Adsorbate-adsorbate interactions are considered for all possible reaction intermediate pairs. The following equations are adopted to describe the adsorption energy as a function of coverage[35, 36]

$$E_i(\theta_i) = \begin{cases} E_i^0 & \text{when } |\theta| \le \theta_0 \\ E_i^0 + \sum_j f\varepsilon_{ij}\theta_j & \text{when } |\theta| > \theta_0 \end{cases} \quad (17)$$

where $E_i(\theta_i)$ denotes the differential adsorption energy of species i at coverage θ_i, E_i^0 the differential adsorption energy at low coverage limit, θ_0 the threshold coverage (0.25 monolayer (ML) in this work), $|\theta|$ the sum of the surface coverages of all adsorbates except H* (the H* coverage is excluded to account for H* being much smaller than CO and therefore has little effect on determining the strength of the interactions), ε_{ij} the cross-interaction parameter between species i and j, f the fractional coverage, which can be calculated as $f = \frac{|\theta| - \theta_0}{|\theta|}$.

As shown above, the interactions are significant only when adsorbate coverages exceed a threshold of about 0.25 ML, and CO* is the only intermediate that has a coverage above this threshold in the potential range of interest, therefore only the interactions between CO* and other intermediates affect the energetics. The energetics of intermediates and TSs are therefore all functions of coverage.

The barriers and reaction energies could thus shift accordingly at high surface coverage. We have explicitly parameterized the CO self-interaction and its cross-interaction parameters with the species in the rate-limiting steps. For the other intermediates that are not in the rate-limiting steps, their interaction parameters do not change the kinetic results significantly. We therefore have assumed the interaction parameters to be the same due to the similar sizes of molecules.

The adsorbate cross-interaction parameters were listed below.

$\epsilon_{CO^*, CO^*} = 2.47$

$\epsilon_{CO^*, H^*} = 0.73$

$\epsilon_{CO^*, H\text{-}ele^*} = 0.79$

$\epsilon_{CO^*, H2\text{-}ele^*} = 0.51$

$\epsilon_{CO^*, H\text{-}H^*} = 1.16$

$\epsilon_{CO^*, H\text{-}CO\text{-}ele^*} = \epsilon_{CO^*, CHO^*} = 3.33$

$\epsilon_{CO^*, CO\text{-}H\text{-}ele^*} = \epsilon_{CO^*, COH^*} = \epsilon_{CO^*, COH\text{-}H^*} = 2.84$

$\epsilon_{CO^*, C^*} = \epsilon_{CO^*, C\text{-}H\text{-}ele^*} = \epsilon_{CO^*, OCCO\text{-}H\text{-}ele^*} = \epsilon_{CO^*, OCCO^*} = \epsilon_{CO^*, OCCOH^*} = \epsilon_{CO^*, C\text{-}CO^*} = \epsilon_{CO^*, OC\text{-}C^*} = \epsilon_{CO^*, OC\text{-}CH^*} = \epsilon_{CO^*, OCC\text{-}H\text{-}ele^*} = \epsilon_{CO^*, CCO^*} = \epsilon_{CO^*, CHCO^*} = \epsilon_{CO^*, H\text{-}CO^*} = \epsilon_{CO^*, CH\text{-}H^*} = \epsilon_{CO^*, CH2\text{-}H^*} = \epsilon_{CO^*, CH3\text{-}H^*} = 2.47$

$\epsilon_{CO^*, CH^*} = \epsilon_{CO^*, CH\text{-}H\text{-}ele^*} = 1.85$

$\epsilon_{CO^*, OH^*} = 1.60$

$\epsilon_{OH^*, OH^*} = 1.03$

CH_2*, CH_3*, and CHOH* were assumed to have same interactions as those of CO*. All unlisted $\epsilon_{i,j}$ are assumed to be zero.

Supplementary Note 7: CO* overbinding correction

We have applied an overbinding correction to CO adsorption energies on strong-binding metals (Ir, Rh, Pt, Pd, and Ni) due to generalized gradient approximations (GGA) functionals generally positioning the unfilled 2π* orbital at too low energy. The correction is based on the vibrational frequency of the internal CO stretch mode of *CO, relative to the frequency in vacuum.[37] The vibrational frequencies can be found in **Table S8**.

Table S8. The ν_{CO} for overbinding correction. Harmonic vibrational frequencies for the CO internal stretch mode (ν_{CO}), ZPE, and overbinding correction ($E_{corr} = 1.8 - 0.0008 \times \nu_{CO}$) found for adsorption onto different metals and adsorption sites. The overbinding correction was only applied to strong-binding metals of Pd, Pt, Rh, Ni, and Ir.

Surface orientation	Metal	ν_{CO} (cm^{-1})			ZPE (eV)			E_{corr} (eV)		
		ontop	bridge	*hcp* hollow	ontop	bridge	*hcp* hollow	ontop	bridge	*hcp* hollow
111	Au	2065		1845	0.17		0.16			
	Cu	2020		1814	0.18		0.16			
	Pd	2026		1769	0.19		0.19	0.18		0.38
	Pt	2049		1755	0.21		0.19	0.16		0.40
	Rh	1984		1728	0.20		0.18	0.21		0.42
	Ni	2001		1753	0.20		0.18	0.20		0.40
	Ir	1999		1704	0.22		0.18	0.20		0.44
211	Ag	2038	1967		0.15	0.15				
	Au	2054	1886		0.17	0.18				
	Cu	2026	1898		0.18	0.17				
	Pd	2021	1867		0.19	0.19		0.18	0.31	
	Pt	2031	1843		0.20	0.20		0.18	0.33	
	Rh	1973	1822		0.20	0.19		0.22	0.34	
	Ni	1994	1855		0.20	0.19		0.21	0.32	
	Ir	1980	1808		0.21	0.19		0.22	0.35	
100	Au	2066			0.17					
	Cu	2079	1942	1766	0.17	0.17	0.14			
	Pd	2015	1860	1687	0.18	0.19	0.16	0.19	0.31	0.45
	Pt	2041	1842	1676	0.20	0.20	0.15	0.17	0.33	0.46
	Rh	1971	1819	1642	0.20	0.19	0.16	0.22	0.34	0.49
	Ni	1990	1835	1617	0.19	0.19	0.17	0.21	0.33	0.51
	Ir	1993		1622	0.22		0.16	0.21		0.50

After overbinding correction, the theoretically calculated CO binding energies (E_{CO*}^{theo}, ZPE and E_{corr} added) show better agreement with the experimental CO binding energies measured at high-vacuum conditions (E_{CO*}^{exp}) (**Figure S6**). The mean absolute error (MAE) decreases from 0.21 eV to 0.17 eV through overbinding correction. Moreover, with the overbinding correction, we can predict the CO binding sites on strong-binding metals of Pt

and Rh correctly: before correction, the hcp hollow sites are predicted for CO adsorption; after correction, the ontop sites are predicted, which have also been experimentally validated.

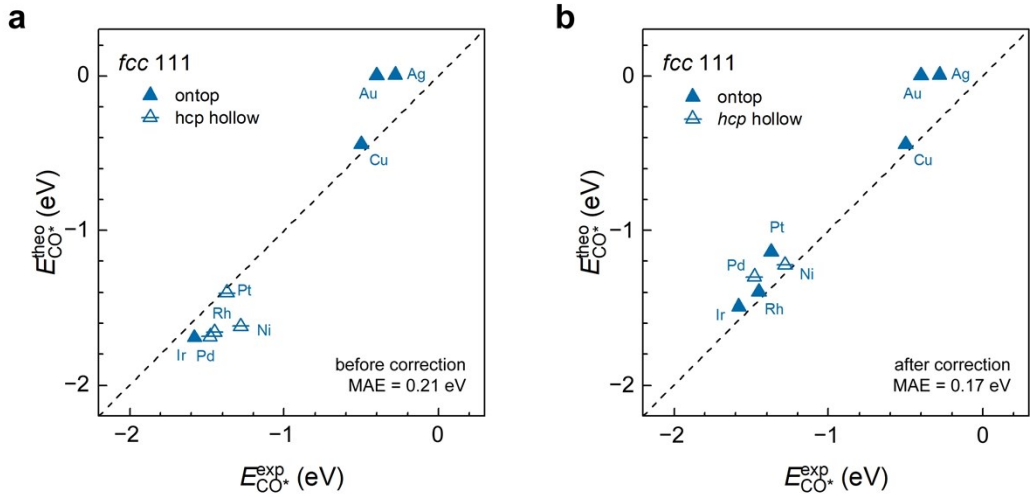

Figure S6. Comparison between experimental and theoretical CO binding energies. (**a**) Before correction and (**b**) after correction. The theoretical CO binding energies are obtained using a correction for overbinding, according to $E_{corr} = 1.8 - 0.0008 \times \nu_{CO}$ and including ZPE. The experimental CO binding energies were directly adopted from Abild-Pedersen et al.[37].

All relaxed structures and energetics are available on the Catalysis-Hub database.[38] Adsorption energies for building selectivity maps in **Figure 6** and **Figures S18–S22** could be found in **Table S9**. All computational data linked to the list of corresponding electronic energies has been released as part of the Catalysis-hub.org repository[38] under https://www.catalysis-hub.org/publications/PengThe2020.

Table S9. Energetics of all species on various metals and intermetallics. All adsorption energies *G* (in eV) are referenced to CO, H_2O, and H_2 (ref). The *G* of an adsorbate are identified as reaction free energy change (ΔG) of the formation reaction from reference gas-phase molecules. Note that the solvation corrections are not applied herein.

fcc(111)	Ag	Au	Cu	Pd	Pt	Rh	Ni	Ir
CO*	0.49	0.48	0.05	−0.81	−0.64	−0.90	−0.73	−1.00
H*		0.66	0.21	−0.26	−0.11	−0.17	−0.37	
C*	3.84	2.82	2.34	0.04	0.12	−0.32	0.13	−0.26
CH*	2.52	1.69	1.21	−0.52	−0.73	−0.86	−0.57	
CCO*	0.96	0.84	0.11	−0.50	−0.61	−0.94	−0.86	
fcc(211)	Ag	Au	Cu	Pd	Pt	Rh	Ni	Ir
CO*	0.30	0.19	−0.20	−0.79	−0.97	−0.96	−0.84	−1.38
H*	0.49	0.38	0.08	−0.16	−0.30	−0.26	−0.24	
C*	3.14	2.75	1.32	−0.69	−0.05	−0.78	−0.83	−0.47
CH_2*	1.14	0.44	0.28	−0.46	−0.99	−0.83	−0.62	
fcc(100)	Ag	Au	Cu	Pd	Pt	Rh	Ni	Ir

CO*	0.35	0.25	−0.12	−0.77	−0.92	−0.98	−0.76	−1.27
COH*			1.18	−0.14		−0.67	−0.55	
C*	2.87	2.50	0.95	−0.80	−0.56	−1.24	−1.18	−1.12
CH*	1.86		0.36	−0.57		−1.24	−1.18	
CCO*	0.61		−0.42	−0.68		−1.43	−1.42	
Various Cu facets	(110)	(310)	(511)	(711)	(521)	(621)	(653)	(111)-SV
CO*	−0.24	−0.28	−0.13	−0.14	−0.27	−0.31	−0.26	−0.09
C*	1.57	1.08	1.16	1.06	1.28	1.04	1.39	1.63
$L1_2$ A_3B intermetallics	Cu_3Ag	Cu_3Al	Cu_3Zn	Ag_3Cu				
CO*	−0.11	0.00	−0.12	−0.23				
C*	1.54	0.21	1.47	1.62				
$L1_0$ AB intermetallics	CuAg	CuAl	CuZn					
CO*	−0.14	0.17	−0.02					
C*	1.30	0.04	1.40					
Ni-Ga	Ni_3Ga (100)	Ni_5Ga_3 (100)	Ni_5Ga_3 (221)	Ni_5Ga_3 (111)				
CO*	−0.68	−0.63	−0.78	−0.57				
C*	0.85	1.05	0.54	0.39				

2. Supplementary Figures Relevant to the Contents in the Main Text

2.1. Reaction pathways for COR

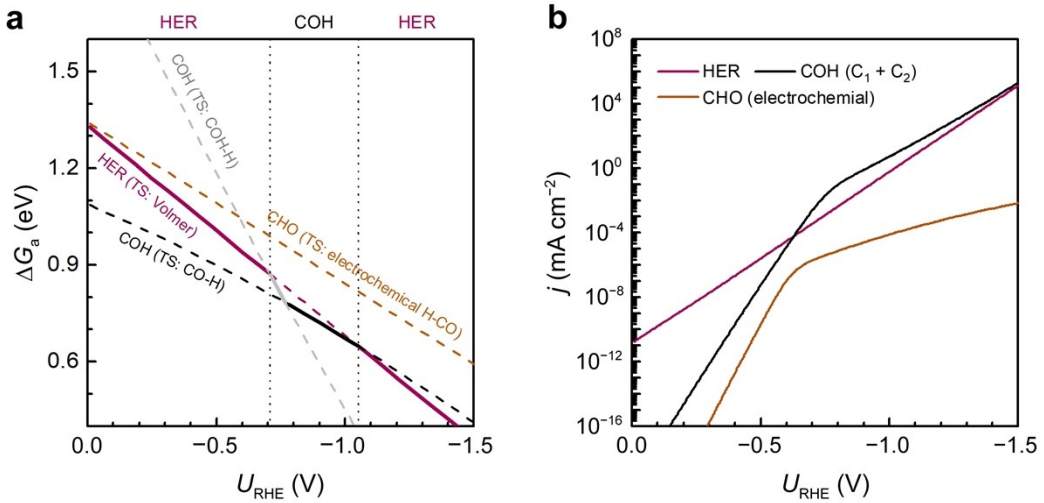

Figure S7. Comparison between hydrogen evolution reaction (HER), the CHO pathway, and the COH pathway under COR conditions at pH = 7. (**a**) Potential (U)-dependent activation energies (ΔG_a) for HER, the CHO pathway, and the COH pathway. The CHO pathway is assumed to be electrochemical. ΔG_a for each reaction equals to $G_{TS:\ Volmer}$ (for HER), $G_{TS:\ H\text{-}CO} - G_{CO*}$ (for the electrochemical CHO pathway), and $G_{TS:\ COH\text{-}H} - G_{CO*}$/$G_{TS:\ CO\text{-}H} - G_{CO*}$ (for the COH pathway), respectively. Due to the different charge-transfer coefficient β (0.65 for the Volmer, 0.5 for H-CO protonation and CO-H protonation, and 0.45 for COH-H protonation), as well as the different degrees affected by the interfacial charge, each ΔG_a exhibits different potential dependency. (**b**) Theoretical polarization curves obtained through microkinetic modeling, showing that even if the CHO formation step is assumed to be electrochemical with an explicitly calculated barrier as in Ref.[9, 39], the CHO pathway is kinetically slower than both HER and the COH pathway on Cu(100). Note that the energetics in (**a**) do not consider the adsorbate-adsorbate interaction while energetics in (**b**) consider, which give a slightly different potential window where the COH pathway dominates over HER.

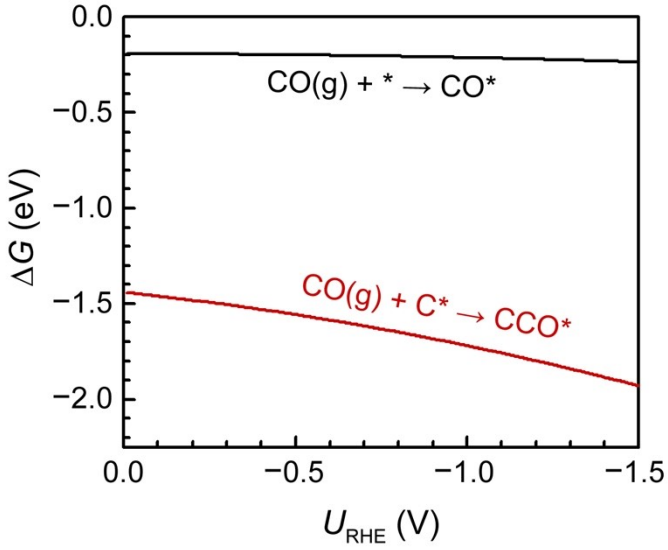

Figure S8. Comparison between CO adsorption and C-CO coupling toward CCO*. Free energy changes as a function of potential (U_{RHE}) for CO adsorption (CO(g) + * → CO*) and CCO formation (CO(g) + C* → CCO*), showing the strong tendency of forming CCO* when C* is present at the surface.

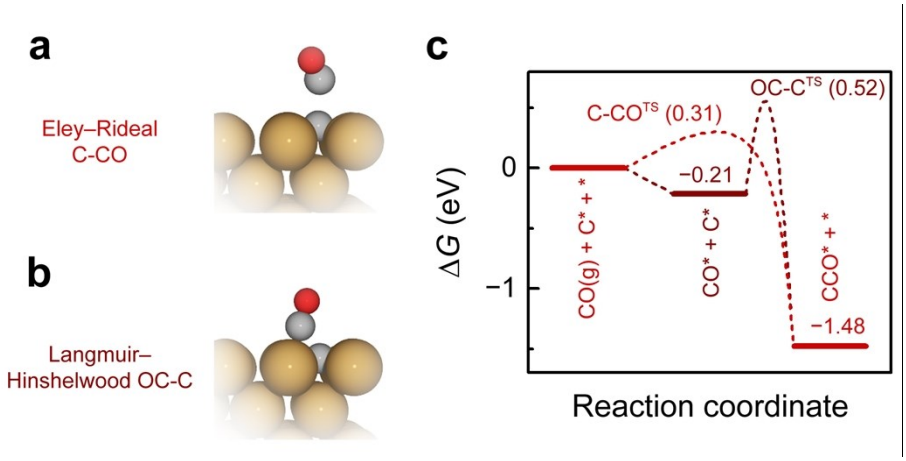

Figure S9. Two mechanisms for C-CO coupling on Cu(100). Optimized atomic configurations of TS structures of C-CO coupling: (**a**) Eley–Rideal mechanism (C* + CO(g) → CCO*, denoted as C-CO) and (**b**) Langmuir–Hinshelwood mechanism (C* + CO* → CCO* + *, denoted as OC-C).[40, 41] (**c**) Gibbs free energy diagrams (FEDs) of C-CO and OC-C coupling, revealing the energetically favored Eley–Rideal pathway. Note that the energetics shown in this figure were obtained without field.

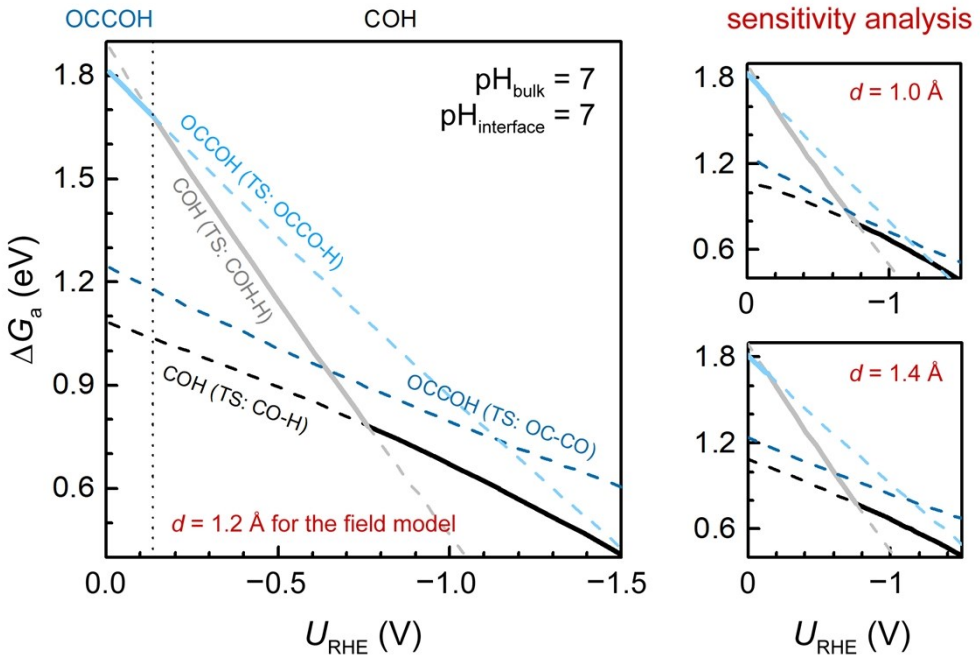

Figure S10. Comparison between the OCCOH and COH pathways under COR conditions at pH = 7. The definition of ΔG_a for each pathway is shown to be: (*black*) COH (TS: CO-H): $G_{\text{TS: CO-H}} - G_{\text{CO*}}$; (*gray*) COH (TS: COH-H): $G_{\text{TS: COH-H}} - G_{\text{CO*}}$; (*blue*) OCCOH (TS: OC-CO): $G_{\text{OCCO*}} - 2G_{\text{CO*}}$; (*azure*) OCCOH (TS: OCCO-H): $G_{\text{TS: OCCO-H}} - 2G_{\text{CO*}}$. All the energetics were obtained using Eq. (3) and Eq. (4) and the parameters in **Table S3** and **Tables S5–S7**. Sensitivity analysis was performed by varying *d* from 1.0 to 1.4 Å and the induced difference in binding energies does not change the general trend that at more negative potentials, the COH/OC-C pathway is more favorable than the OCCOH pathway.

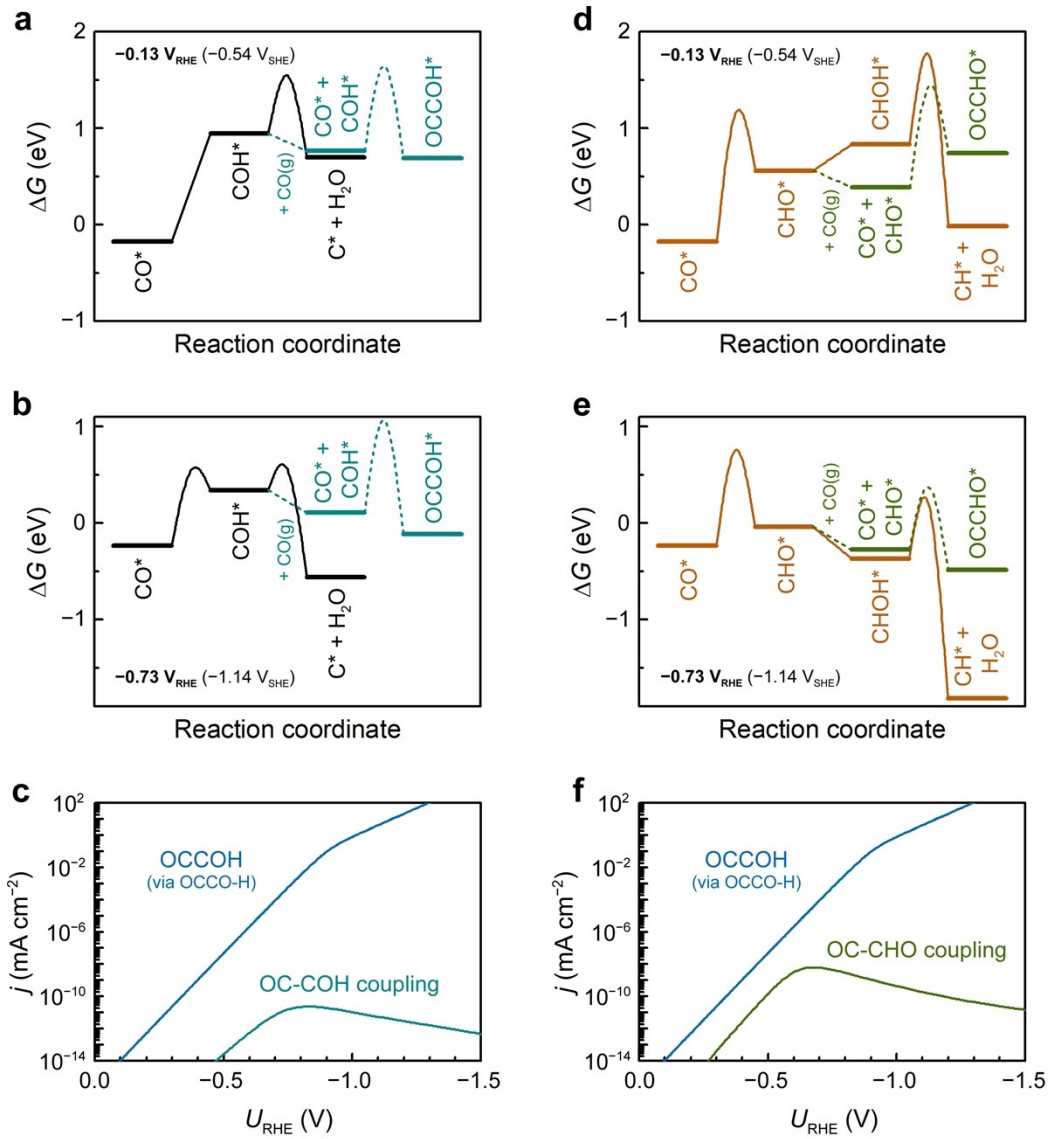

Figure S11. Other early coupling pathways in comparison with OCCOH under COR conditions at pH = 7. FEDs of the OC-COH pathway in comparison with the competing reduction pathway of COH* → C* + H_2O at potentials (**a**) U_{RHE} = −0.13 V and (**b**) U_{RHE} = −0.73 V. (**c**) Simulated reaction rates of OC-COH coupling in comparison with the rate of OCCOH pathway. FEDs of the OC-CHO pathway in comparison with the competing reduction pathway of CHO* → CHOH* → CH* + H_2O at potentials (**d**) U_{RHE} = −0.13 V and (**e**) U_{RHE} = −0.73 V. The OC-CHO coupling barrier (0.65 eV) at U_{RHE} = −0.73 V is comparable to the reported values (0.65–0.70 eV at U_{RHE} > −0.6 V) by Goodpaster et al.[42].(**f**) Simulated reaction rates of OC-CHO coupling in comparison with the rate of OCCOH pathway. The two pathways of OC-COH and OC-CHO coupling become less competitive than the OCCOH pathway because at low overpotentials, the two pathways are mainly limited by the first protonation steps of CO* to either COH* or CHO*, while at high overpotentials, the competing reduction pathways to form C* + H_2O and CH* + H_2O from COH* and CHO* become more favorable than the chemical coupling steps, respectively, leading to downward trends of OC-COH and OC-CHO coupling rates shown in (**c**) and (**f**). Nevertheless, the possibility of forming experimentally obtained minor products such as glyoxal and glycolaldehyde

from OCCHO* as demonstrated by Garza et al.[43] is not excluded. But their formation rates are expected to be significantly lower than formation rates of major C_2 products.

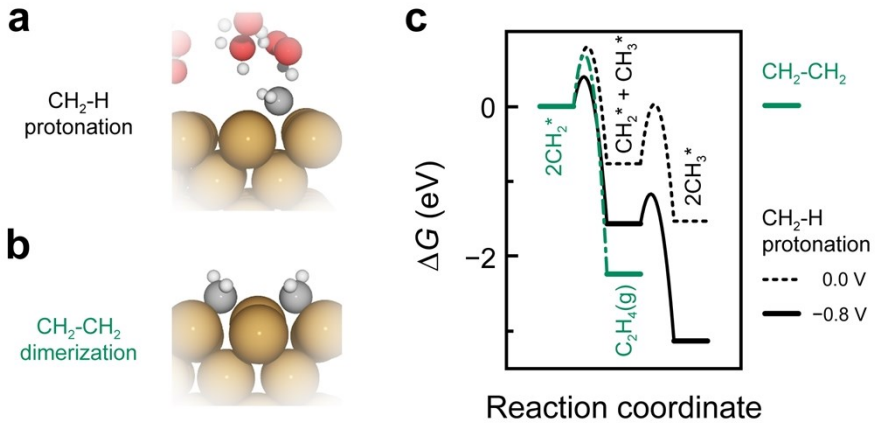

Figure S12. The competition between CH_2-CH_2 dimerization and CH_2-H protonation on Cu(100). Optimized atomic configurations of TS structures: (**a**) CH_2-H protonation (CH_2* + H^+ + e^- → CH_3*) and (**b**) CH_2-CH_2 dimerization ($2CH_2$* → C_2H_4(g) + 2*). (**c**) FEDs of CH_2-CH_2 dimerization and CH_2-H protonation, revealing the energetically favored CH_2-H protonation at negative U_{RHE}.

2.2. Microkinetic model of COR and pH effects

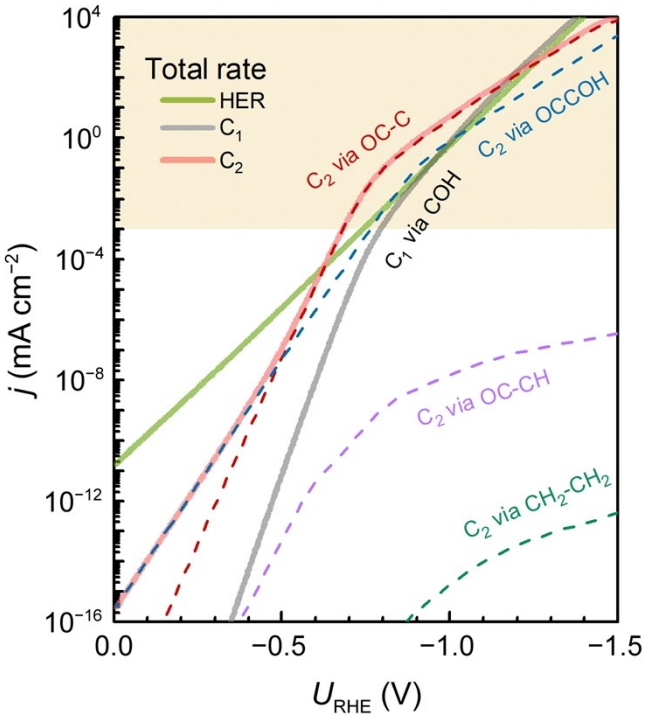

Figure S13. Theoretical partial current densities on Cu(100) (pH = 7). Theoretical polarization curves showing the total rates of HER, C_1, and C_2, as well as the partial contribution of each pathway to the current density (j).

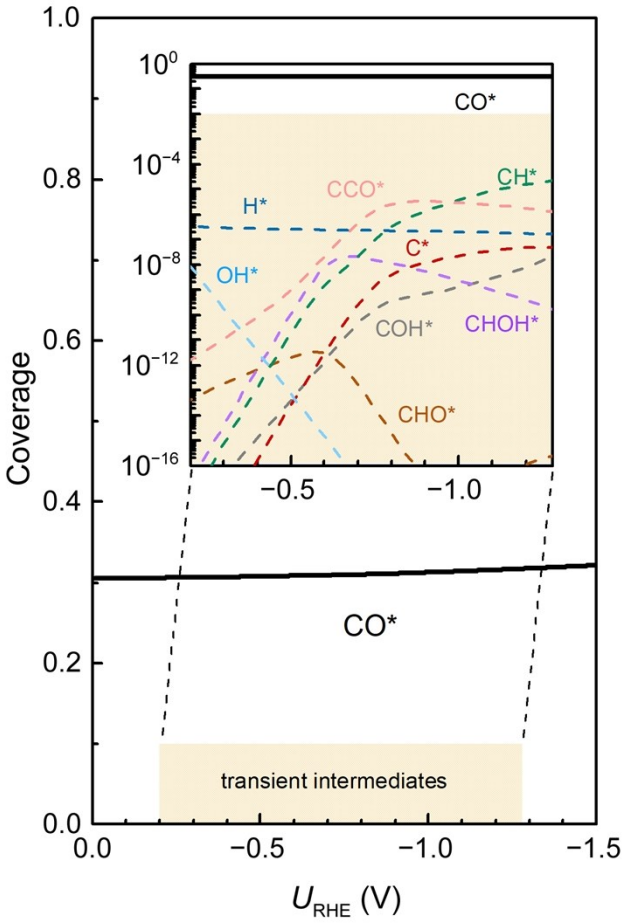

Figure S14. Steady-state coverages of surface species on Cu(100). The coverages of different species are plotted again potential vs. RHE at pH = 7. These coverages correspond to the model shown in **Figure 3**. CO* is found to be the dominant surface specie within a broad potential range; while H*, COH*, CHO*, C*, CHOH*, CH*, and CCO* are regarded as transient intermediates due to their rapid conversion to more reduced products at negative potentials. The low coverage of COH*/CHO*/CHOH*, along with the corresponding higher coupling barrier than the protonation counterpart, limits the activity of OC-COH, OC-CHO, and OC-CHOH coupling.

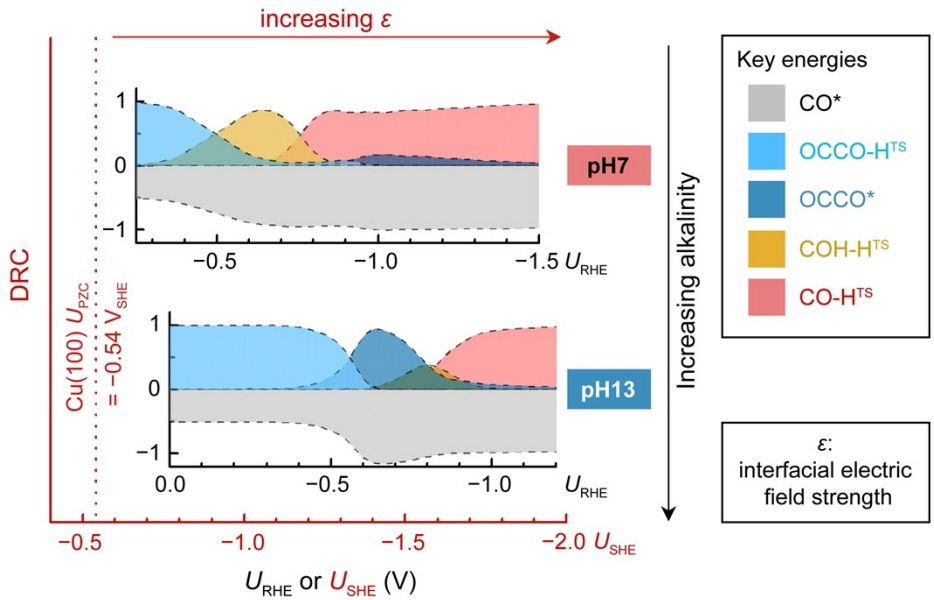

Figure S15. Degree of rate control (DRC) analysis. Simulated DRC of COR at bulk pH7 and bulk pH13. As conceptualized by Campbell et al.,[44, 45] DRC serves as a powerful tool to quantify the magnitude of rate controlling by a certain intermediate or a TS. A positive (negative) value of DRC indicates that the corresponding reaction intermediate or TS needs to be stabilized (destabilized) in order to enhance the rate. The boundary values of 1 and −1 represent full rate control by the intermediates. Key intermediates and TSs are shown in light gray (CO*), azure (OCCO-H^{TS}), blue (OCCO*), yellow (COH-H^{TS}), and red (CO-H^{TS}), respectively. OCCO-H^{TS}, COH-H^{TS}, and CO-H^{TS} refer to TSs of OCCO-H, COH-H, and CO-H protonations, respectively. This figure clearly shows that the rate-determining step of COR is initially OCCO-H protonation and then changes into COH-H protonation and CO-H protonation as the potential goes negative at pH7. *Videlicet*, the dominant COR pathway shifts from the OCCOH to the COH/OC-C with increasing overpotential. At pH13, the change in RDS follows the same trend but the U_{SHE} for the pathway transition becomes more negative. If we consider the practical high local pH as illustrated in **Figures S16–S17**, the RDS in both bulk pH7 and bulk pH13 will remain as the first electron transfer step in each pathway (OCCO-H in the OCCOH pathway and CO-H in the COH/OC-C pathway). This observation is consistent with the Tafel slopes of $CO_{(2)}R$ measured experimentally.

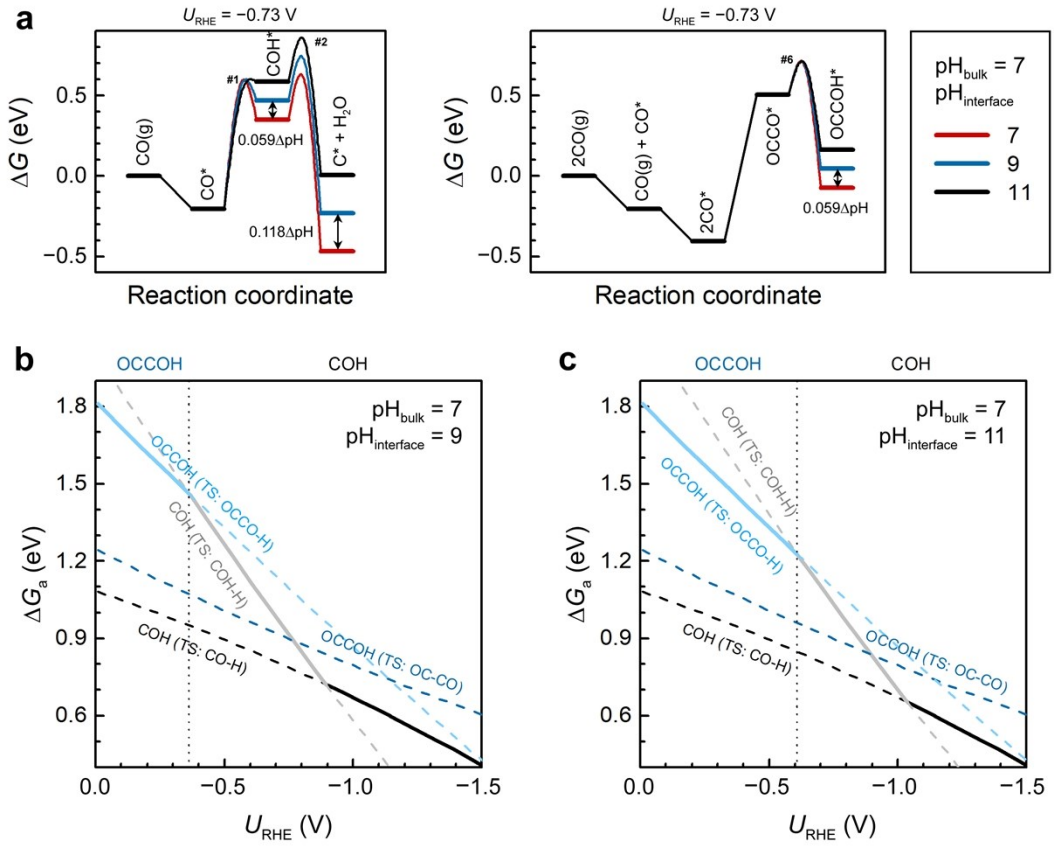

Figure S16. Local pH ($pH_{interface}$) effects on energetics of key steps. (**a**) FEDs (at U_{RHE} = −0.73 V) of key steps: (*left*) the COH pathway (CO* → COH* → C* + H_2O* → …); (*right*) the OCCOH pathway toward C_2 (CO* → OCCO* → OCCOH* → …). Various local pH conditions are referred to red ($pH_{interface}$ = 7), blue ($pH_{interface}$ = 9), and black ($pH_{interface}$ = 11) colors, respectively. To elucidate the pH effect on each final state of protonation step, water as the proton source is explicitly included in corresponding initial state and thus hydroxide anion (OH^-) is present in the final state. According a previous study (also elucidated in **Supplementary Note 5** and **Figure S4**),[9] the electrochemical barrier (ΔG_a) of alkaline protonation steps is dependent on the U_{SHE} while reaction energy (ΔG_{rxn}) is U_{RHE} -dependent. Taking CO-H protonation to form COH* as an example, the red and blue profiles show the same ΔG_a since they are collected at the same bulk pH of 7 and the absolute potential at the working electrode is measured from the reference electrode contacting with the pH-buffered bulk electrolyte (pH_{bulk} = 7); in contrast, the blue profile shows a higher final state by an amount of 0.059ΔpH (ΔpH = 9−7 = 2) due to the higher OH^- concentration than that of the neutral condition (the red one). Comparison between the OCCOH and COH pathways under COR conditions at (**b**) $pH_{interface}$ = 9 and (**c**) $pH_{interface}$ = 11, respectively. The definition of ΔG_a for each pathway is shown to be: (*black*) COH (TS: CO-H): $G_{TS:\,CO\text{-}H} - G_{CO*}$; (*gray*) COH (TS: COH-H): $G_{TS:\,COH\text{-}H} - G_{CO*}$; (*blue*) OCCOH (TS: OC-CO): $G_{OCCO*} - 2G_{CO*}$; (*azure*) OCCOH (TS: OCCO-H): $G_{TS:\,OCCO\text{-}H} - 2G_{CO*}$.

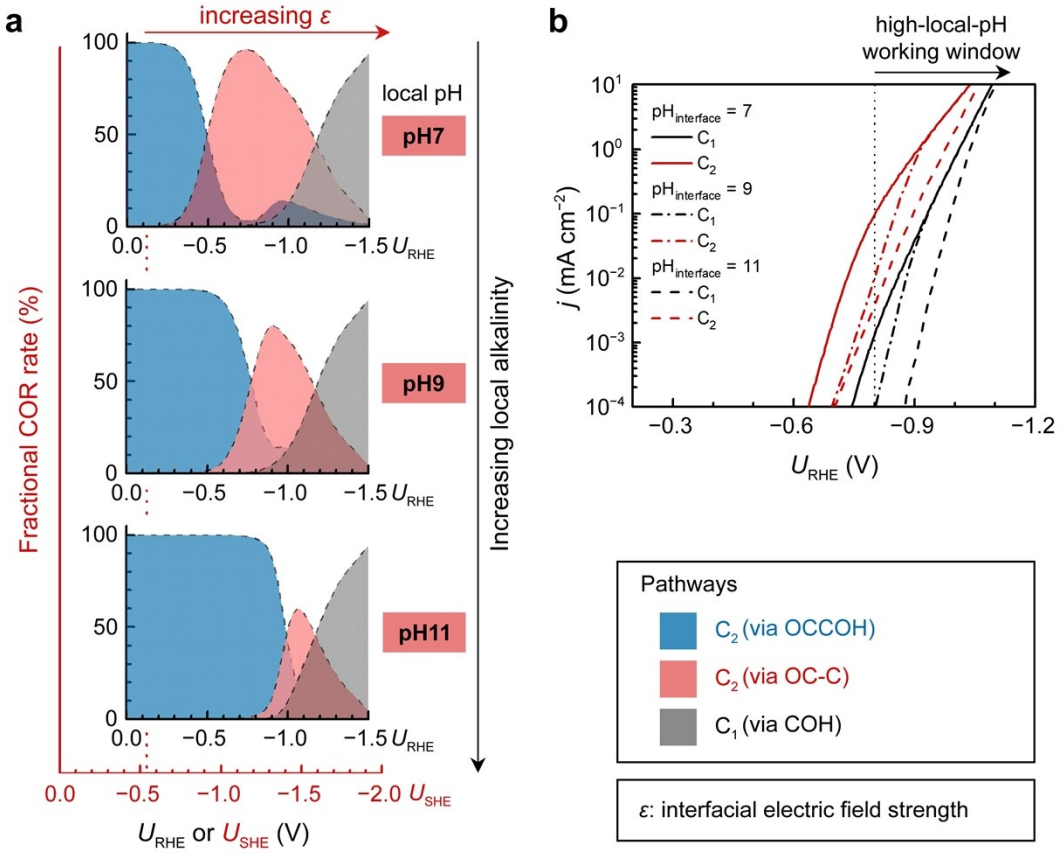

Figure S17. Product distributions and polarization curves of $CO_{(2)}R$ on Cu(100) in bulk neutral electrolyte (pH_{bulk} = 7) under different local pH ($pH_{interface}$) conditions. (**a**) Fractional COR rates (by normalizing to the total COR rate) from three pathways; OCCOH to C_2, OC-C to C_2, and COH to C_1. Pathways are shown in blue, red, and gray, respectively. Different $pH_{interface}$ conditions are considered with $pH_{interface}$ varying from 7 to 9, and to 11. The local alkalinity increases from top to the bottom. (**b**) Theoretical polarization curves. $U_{RHE} < -0.8$ V was suggested as the major potential window where high current density of $> 10^2$ mA cm^{-2} was obtained and a high local pH was induced.[46, 47]

2.3. Selectivity maps with G_{CO*} and G_{C*} as descriptors

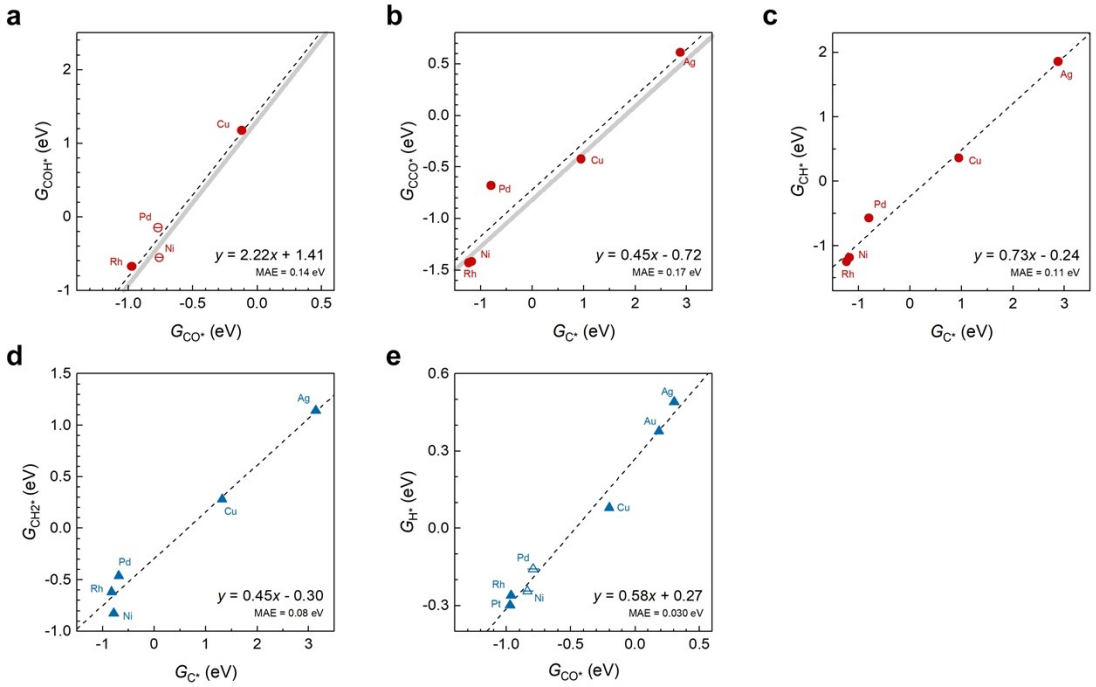

Figure S18. (100) and (211) energetic scaling lines with descriptors of G_{CO*} and G_{C*}. (**a**) G_{COH*}, (**b**) G_{CCO*}, (**c**) G_{CH*}, (**d**) G_{CH2*}, and (**e**) G_{H*}. These scaling lines were used to construct **Figure 6** and **Figures S19, S20**. The strongest adsorption sites were generally adopted: (211) step bridge (sbr) site for H* and CH_2*; (100) four-fold hollow site for C*, COH*, CCO*, and CH*. The adsorption site for CO* depends on the metal: for Ag, Au, Cu, Pt, and Rh, ontop site on both (211) and (100) surfaces; for Pd and Ni, bridge site on the two surfaces. The blue color indicates the (211) scaling lines while the red color indicates the (100) scaling lines. Note that the 5*d* metals Au and Pt, are excluded to construct the (100) scaling lines as their strongest binding sites for COH* and CH* are the (111) *hcp* hollow sites. Besides, the Ag(100) is excluded for constructing these scaling lines using G_{CO*} as the descriptor because Ag(100) do not adsorb CO. The light grey lines in **a** and **b** show the solvation effects on adsorption energies of COH* and CCO*.

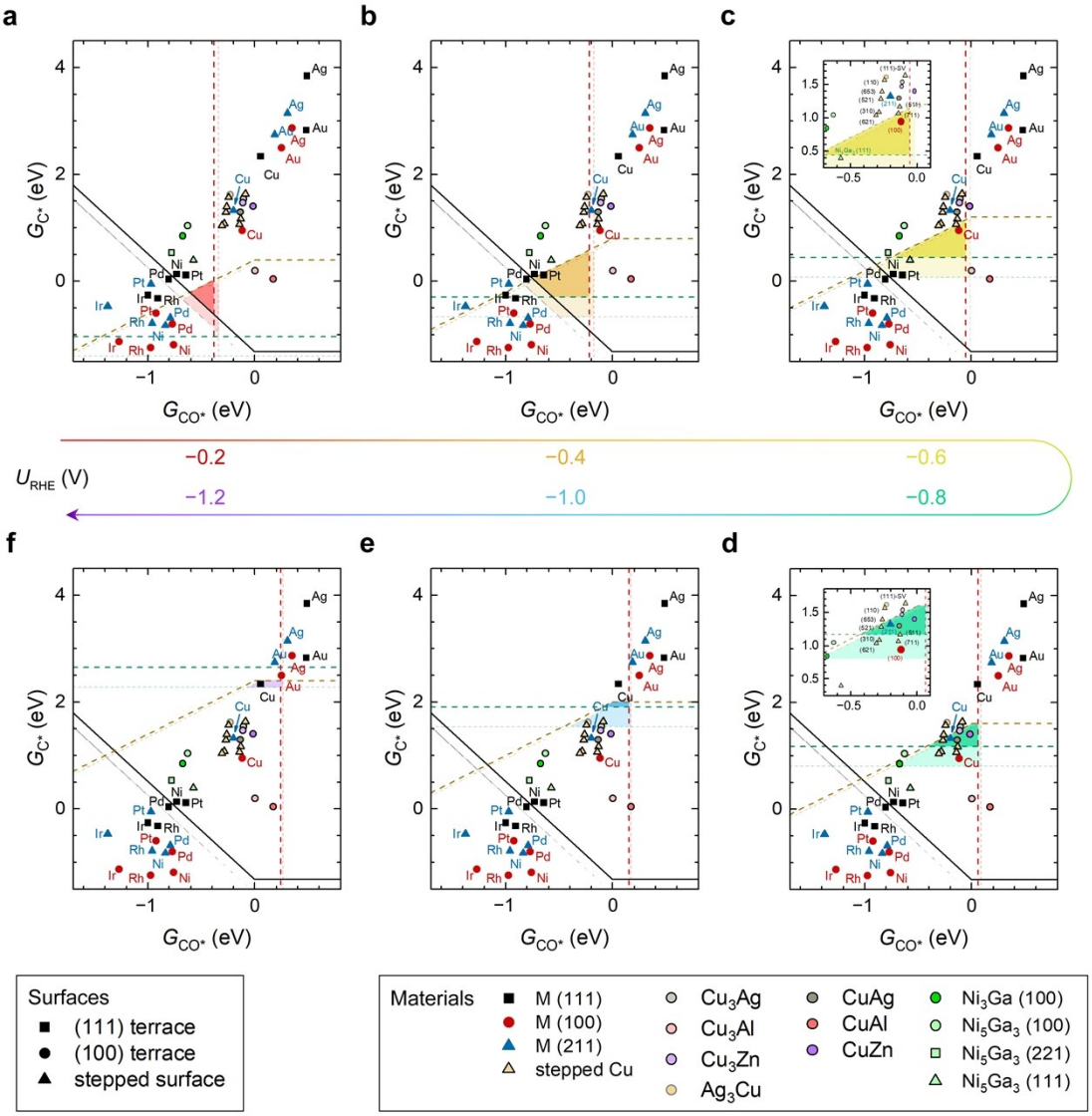

Figure S19. (G_{CO^*}, G_{C^*}) selectivity maps toward C_2 products. C_2-selective regions are highlighted at various potentials. Similar to **Figure 6**, the light colors refer to solvation-corrected energetics. Various metallic and intermetallic systems are shown with their denoted symbols as indicated in the Materials legend and the denoted symbols for their surface structures are indicated in the Surfaces legend. Boundary lines are shown as dashed lines for electrochemically driven processes, or solid lines for the potential-independent C-CO coupling process. The thermodynamic boundaries are exactly the same as in **Figure 6** and the U in the equations is referenced to RHE. These maps could rationalize several experimental observations:

- Ni-Ga intermetallics (especially the stepped Ni_5Ga_3 (111) surface) are suggested to produce C_{2+} products within a U_{RHE} window of −0.5 V to −0.7 V (estimated from (**b**)–(**d**)), which is in good accordance with the experiments by Lewis and coworkers.[48]
- The intermetallic compounds such as Cu_3Ag, CuAg, Cu_3Zn, and CuZn are also predicted to possess comparable C_2 selectivity to pure Cu within an estimated U_{RHE} window of −0.7 V to −0.9 V ((**c**)–(**e**)). These compounds (in the same or similar composition) have been validated in recent experimental advances[49-52] to show comparable or enhanced C_{2+} production from $CO_{(2)}$.
- The comparison between Cu(111) and Cu(111)-SV (inset in (**d**)) could serve as a rough

explanation why defects on close-packed Cu surfaces to create binding sites that stabilize the key intermediate of C* and so allows C_1/C_2 production at lower overpotential than Cu(111). In a recent work on quantum-dot derived Cu nanoparticles, Liu et al. explicitly observed single vacancy on (111) surfaces and demonstrated the enhanced C_2 selectivity on such material.[53] Our theoretical model exactly agrees with their experiments.

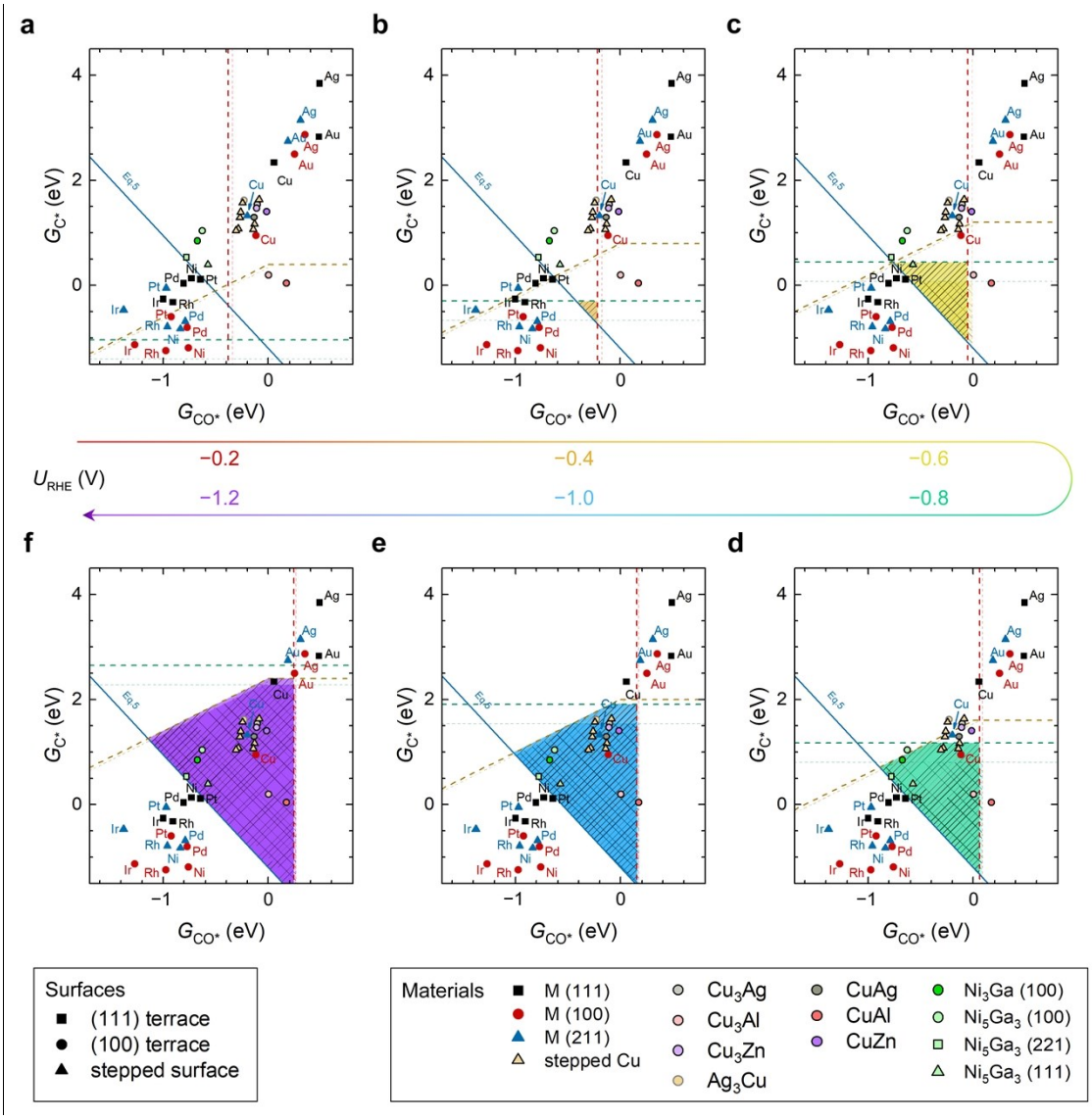

Figure S20. (G_{CO^*}, G_{C^*}) selectivity maps toward C_1 (CH_4) products. C_1-selective regions are highlighted at various potentials. Similar to **Figure 6**, the light-color regions with right slashes refer to solvation-corrected energetics; while the dark-color regions with left slashes refer to vacuum-level energetics. Various metallic and intermetallic systems are shown with their denoted symbols as indicated in the Materials legend and the denoted symbols for their surface structures are indicated in the Surfaces legend. Boundary lines are shown as dashed lines for electrochemically driven processes. The potential-dependent thermodynamic boundaries are exactly the same as in **Figure 6** and the U in the equations is referenced to RHE, but the independent boundary (the solid line) changes Eq. 3 (C-CO coupling vs. CO adsorption) to Eq. 5 (CH protonation to Volmer). The Eq. 5 is expressed as $G_{CH^*} + G_{H^*} = G_{CH2^*}$, which is the thermal-neutral condition for CH protonation

(CH* + H^+ + e^- → CH_2*) and the Volmer (H^+ + e^- + * → H*). Strong binding metals possess more negative (G_{CH*} + G_{H*}) than G_{CH2*} and thus are prone to catalyze HER over CH_4 production. The closer are materials in the C_1-selective regions to the thermodynamic boundaries of Eq. 5, the more dominant HER will be observed. These maps could rationalize several experimental observations:

- Despite the minor hydrocarbon production on Ni-Ga intermetallics (especially the stepped Ni_5Ga_3 (111) surface), terrace-like Ni_5Ga_3 (221) surface is quite close to the thermodynamic boundary of Eq. 5 and thus HER will be quite dominant, which is in good accordance with the observed experimental phenomena: more than 90% FE for HER.[48]
- Unlike Cu-rich intermetallic compounds, Ag electrodes modified by a small amount of Cu (less than 50% surface coverage and thus exemplified as a Cu-poor intermetallic of Ag_3Cu) were demonstrated for selective CH_4 production at U_{RHE} < −1.1 V,[54] which is exactly rationalized by our model ((**e**)–(**f**)).

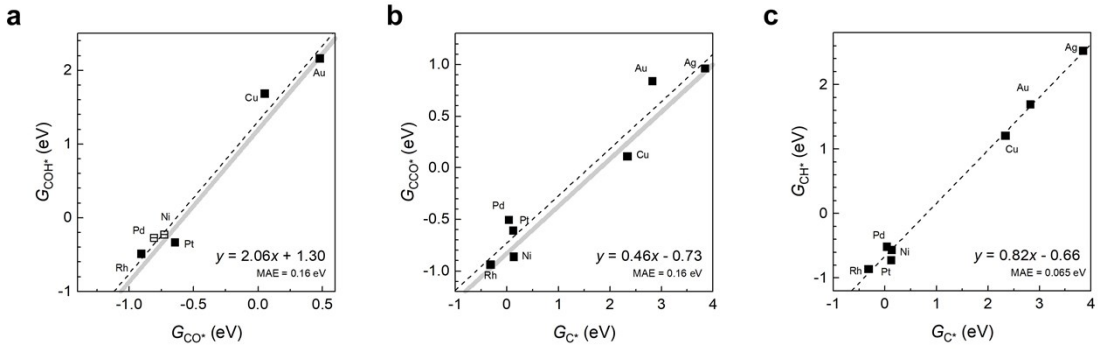

Figure S21. (111) energetic scaling lines with descriptors of G_{CO*} and G_{C*}. (**a**) G_{COH*}, (**b**) G_{CCO*}, and (**c**) G_{CH*}. These scaling lines were used to construct **Figure S22**. The adsorption site for CO* depends on the metal: for Ag, Au, Cu, Pt, and Rh, ontop site; for Pd and Ni, *hcp* hollow site. The Ag(111) is excluded for constructing these scaling lines using G_{CO*} as the descriptor because Ag(111) do not adsorb CO. The light grey lines in **a** and **b** show the solvation effects on adsorption energies of COH* and CCO*.

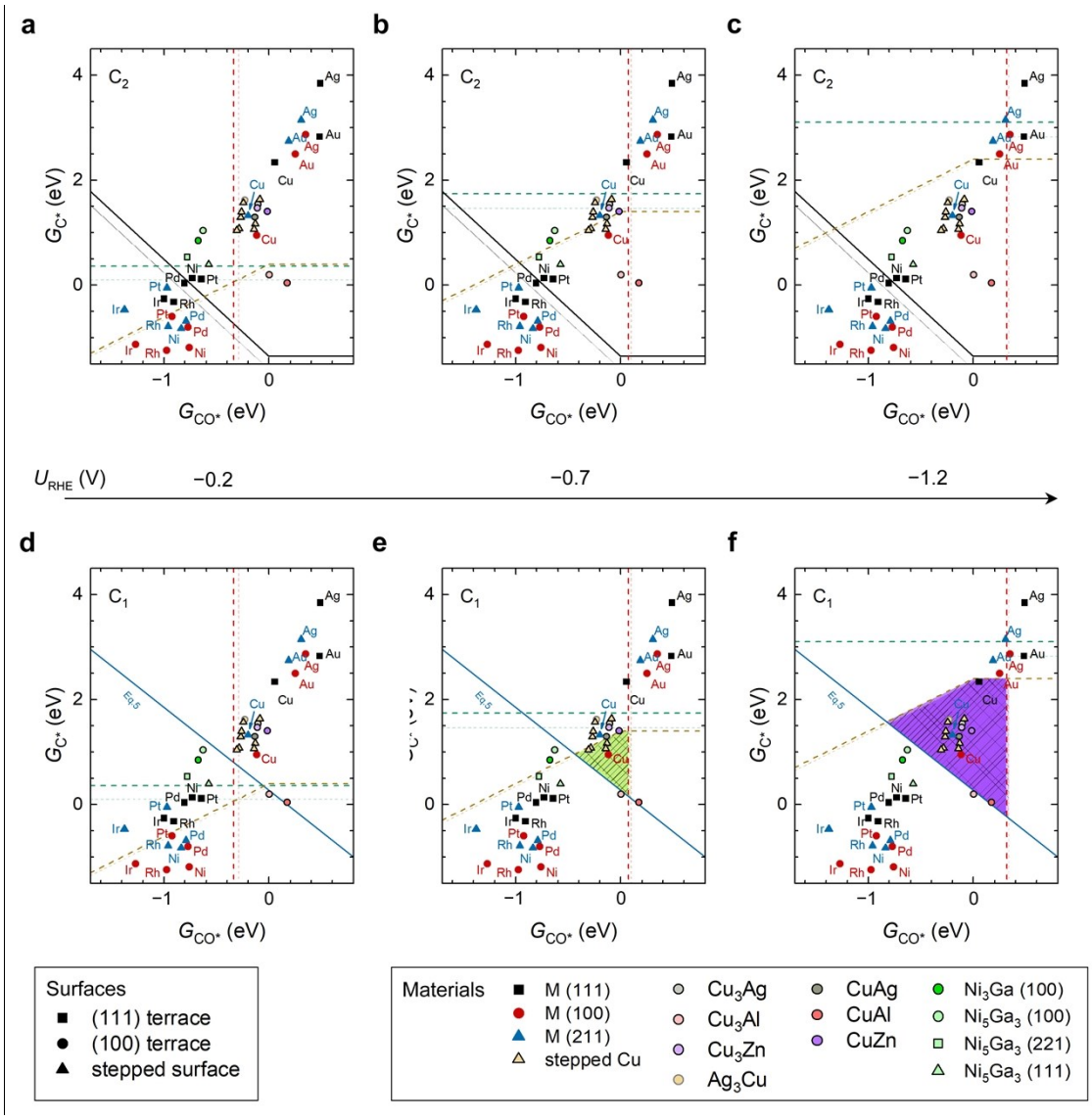

Figure S22. (G_{CO*}, G_{C*}) selectivity maps based on (111) energetic scaling lines. (**a–c**) C_2 selectivity at varying potentials. (**d–f**) C_1 selectivity at varying potentials. All the details are the same as in **Figures S19, S20** but the thermodynamic boundaries were constructed based on (111) energetic scaling lines. Specifically, the (100) energetic scaling lines shown in **Figure S18a–c** were replaced by the (111) energetic scaling lines shown in **Figure S21a–c**. The comparison between these maps with **Figures S19, S20** clearly show the significant shift of thermodynamic boundary defined by Eq. 4 (CCO formation vs. CH formation). This shift renders three-fold hollow site a poor catalytic site motif for selective C_2 production. Thus, engineering four-fold hollow site becomes a key criterion for C_2-selective catalyst design.

3. Supplementary References

1. P. Giannozzi, S. Baroni, N. Bonini, M. Calandra, R. Car, C. Cavazzoni, D. Ceresoli, G. L. Chiarotti, M. Cococcioni, I. Dabo, A. Dal Corso, S. de Gironcoli, S. Fabris, G. Fratesi, R. Gebauer, U. Gerstmann, C. Gougoussis, A. Kokalj, M. Lazzeri, L. Martin-Samos, N. Marzari, F. Mauri, R. Mazzarello, S. Paolini, A. Pasquarello, L. Paulatto, C. Sbraccia, S. Scandolo, G. Sclauzero, A. P. Seitsonen, A. Smogunov, P. Umari and R. M. Wentzcovitch, *J. Phys-Condens. Mat.*, 2009, **21**, 395502.
2. S. R. Bahn and K. W. Jacobsen, *Computing in Science & Engineering*, 2002, **4**, 56-66.
3. J. Wellendorff, K. T. Lundgaard, A. Mogelhoj, V. Petzold, D. D. Landis, J. K. Nørskov, T. Bligaard and K. W. Jacobsen, *Phys. Rev. B*, 2012, **85**, 235149.
4. H. J. Monkhorst and J. D. Pack, *Phys. Rev. B*, 1976, **13**, 5188-5192.
5. Z. W. Ulissi, M. T. Tang, J. P. Xiao, X. Y. Liu, D. A. Torelli, M. Karamad, K. Cummins, C. Hahn, N. S. Lewis, T. F. Jaramillo, K. R. Chan and J. K. Nørskov, *ACS Catal.*, 2017, **7**, 6600-6608.
6. M. T. Tang, Z. W. Ulissi and K. R. Chan, *J. Phys. Chem. C*, 2018, **122**, 14481-14487.
7. A. A. Peterson, F. Abild-Pedersen, F. Studt, J. Rossmeisl and J. K. Nørskov, *Energy Environ. Sci.*, 2010, **3**, 1311-1315.
8. Y. Hori, A. Murata and R. Takahashi, *Journal of the Chemical Society-Faraday Transactions I*, 1989, **85**, 2309-2326.
9. X. Y. Liu, P. Schlexer, J. P. Xiao, Y. F. Ji, L. Wang, R. B. Sandberg, M. Tang, K. S. Brown, H. J. Peng, S. Ringe, C. Hahn, T. F. Jaramillo, J. K. Nørskov and K. R. Chan, *Nat. Commun.*, 2019, **10**, 32.
10. T. Ludwig, J. A. Gauthier, K. S. Brown, S. Ringe, J. K. Nørskov and K. Chan, *J. Phys. Chem. C*, 2019, **123**, 5999-6009.
11. J. H. Montoya, C. Shi, K. Chan and J. K. Nørskov, *J. Phys. Chem. Lett.*, 2015, **6**, 2032-2037.
12. J. K. Nørskov, F. Studt, F. Abild-Pedersen and T. Bligaard, *Fundamental Concepts in Heterogeneous Catalysis*, 2014.
13. K. Jiang, R. B. Sandberg, A. J. Akey, X. Y. Liu, D. C. Bell, J. K. Nørskov, K. R. Chan and H. T. Wang, *Nat. Catal.*, 2018, **1**, 111-119.
14. S. Ringe, E. L. Clark, J. Resasco, A. Walton, B. Seger, A. T. Bell and K. Chan, *Energy Environ. Sci.*, 2019, **12**, 3001-3014.
15. D. C. Grahame, *Chem. Rev.*, 1947, **41**, 441-501.
16. J. A. Gauthier, C. F. Dickens, H. H. Heenen, S. Vijay, S. Ringe and K. Chan, *Journal of Chemical Theory and Computation*, 2019, **15**, 6895-6906.
17. S. Trasatti and E. Lust, *Modern Aspects of Electrochemistry*, Springer, 2002.
18. E. Skulason, V. Tripkovic, M. E. Bjorketun, S. Gudmundsdottir, G. Karlberg, J. Rossmeisl, T. Bligaard, H. Jonsson and J. K. Norskov, *J. Phys. Chem. C*, 2010, **114**, 18182-18197.
19. S. Ringe, C. G. Morales-Guio, L. D. Chen, M. Fields, T. F. Jaramillo, C. Hahn and K. Chan, *Nat. Commun.*, 2020, **11**, 33.
20. J. K. Nørskov, J. Rossmeisl, A. Logadottir, L. Lindqvist, J. R. Kitchin, T. Bligaard and H. Jonsson, *J. Phys. Chem. B*, 2004, **108**, 17886-17892.

21. C. Shi, K. Chan, J. S. Yoo and J. K. Nørskov, *Org. Process. Res. Dev.*, 2016, **20**, 1424-1430.
22. J. Resasco, L. D. Chen, E. Clark, C. Tsai, C. Hahn, T. F. Jaramillo, K. Chan and A. T. Bell, *J. Am. Chem. Soc.*, 2017, **139**, 11277-11287.
23. E. L. Clark, S. Ringe, M. Tang, A. Walton, C. Hahn, T. F. Jaramillo, K. Chan and A. T. Bell, *ACS Catal.*, 2019, **9**, 4006-4014.
24. G. Henkelman, B. P. Uberuaga and H. Jonsson, *J. Chem. Phys.*, 2000, **113**, 9901-9904.
25. B. Hammer, Challenges with the currently(correctly) implemented NEB-method. Should ASE revert to the original more robust NEB-formulation with springs?, https://wiki.fysik.dtu.dk/gpaw-files/workshop13/a08.pdf, (accessed Oct. 2016).
26. K. Chan and J. K. Nørskov, *J. Phys. Chem. Lett.*, 2015, **6**, 2663-2668.
27. K. Chan and J. K. Nørskov, *J. Phys. Chem. Lett.*, 2016, **7**, 1686-1690.
28. S. Trasatti, *Pure Appl. Chem.*, 1986, **58**, 955-966.
29. D. Strmcnik, M. Uchimura, C. Wang, R. Subbaraman, N. Danilovic, D. van der Vliet, A. P. Paulikas, V. R. Stamenkovic and N. M. Markovic, *Nat. Chem.*, 2013, **5**, 300-306.
30. P. S. Lamoureux, A. R. Singh and K. R. Chan, *ACS Catal.*, 2019, **9**, 6194-6201.
31. L. Wang, S. A. Nitopi, E. Bertheussen, M. Orazov, C. G. Morales-Guio, X. Y. Liu, D. C. Higgins, K. R. Chan, J. K. Nørskov, C. Hahn and T. F. Jaramillo, *ACS Catal.*, 2018, **8**, 7445-7454.
32. T. J. Schmidt, P. N. Ross and N. M. Markovic, *J. Electroanal. Chem.*, 2002, **524**, 252-260.
33. N. M. Markovic, B. N. Grgur and P. N. Ross, *J. Phys. Chem. B*, 1997, **101**, 5405-5413.
34. A. J. Medford, C. Shi, M. J. Hoffmann, A. C. Lausche, S. R. Fitzgibbon, T. Bligaard and J. K. Nørskov, *Catal. Lett.*, 2015, **145**, 794-807.
35. A. C. Lausche, A. J. Medford, T. S. Khan, Y. Xu, T. Bligaard, F. Abild-Pedersen, J. K. Nørskov and F. Studt, *J. Catal.*, 2013, **307**, 275-282.
36. N. Y. Yang, A. J. Medford, X. Y. Liu, F. Studt, T. Bligaard, S. F. Bent and J. K. Nørskov, *J. Am. Chem. Soc.*, 2016, **138**, 3705-3714.
37. F. Abild-Pedersen and M. P. Andersson, *Surf. Sci.*, 2007, **601**, 1747-1753.
38. K. T. Winther, M. J. Hoffmann, J. R. Boes, O. Mamun, M. Bajdich and T. Bligaard, *Scientific Data*, 2019, **6**, 75.
39. X. Y. Liu, J. P. Xiao, H. J. Peng, X. Hong, K. Chan and J. K. Nørskov, *Nat. Commun.*, 2017, **8**, 15438.
40. P. W. Atkins, *Physical Chemistry*, Oxford University Press, Oxford, 1990.
41. G. Ertl, *Surf. Sci.*, 1994, **299**, 742-754.
42. J. D. Goodpaster, A. T. Bell and M. Head-Gordon, *J. Phys. Chem. Lett.*, 2016, **7**, 1471-1477.
43. A. J. Garza, A. T. Bell and M. Head-Gordon, *ACS Catal.*, 2018, **8**, 1490-1499.
44. C. T. Campbell, *Top. Catal.*, 1994, **1**, 353-366.
45. C. T. Campbell, *ACS Catal.*, 2017, **7**, 2770-2779.
46. J. J. Lv, M. Jouny, W. Luc, W. L. Zhu, J. J. Zhu and F. Jiao, *Adv. Mater.*, 2018, **30**, 1803111.
47. K. L. Yang, R. Kas and W. A. Smith, *J. Am. Chem. Soc.*, 2019, **141**, 15891-15900.

48. D. A. Torelli, S. A. Francis, J. C. Crompton, A. Javier, J. R. Thompson, B. S. Brunschwig, M. P. Soriaga and N. S. Lewis, *ACS Catal.*, 2016, **6**, 2100-2104.
49. E. L. Clark, C. Hahn, T. F. Jaramillo and A. T. Bell, *J. Am. Chem. Soc.*, 2017, **139**, 15848-15857.
50. Y. G. C. Li, Z. Y. Wang, T. G. Yuan, D. H. Nam, M. C. Luo, J. Wicks, B. Chen, J. Li, F. W. Li, F. P. G. de Arguer, Y. Wang, C. T. Dinh, O. Voznyy, D. Sinton and E. H. Sargent, *J. Am. Chem. Soc.*, 2019, **141**, 8584-8591.
51. D. Ren, B. S. H. Ang and B. S. Yeo, *ACS Catal.*, 2016, **6**, 8239-8247.
52. D. Ren, J. Gao, L. F. Pan, Z. W. Wang, J. S. Luo, S. M. Zakeeruddin, A. Hagfeldt and M. Gratzel, *Angew. Chem. Int. Ed.*, 2019, **58**, 15036-15040.
53. M. Liu, M. X. Liu, X. M. Wang, S. M. Kozlov, Z. Cao, P. De Luna, H. M. Li, X. Q. Qiu, K. Liu, J. H. Hu, C. K. Jia, P. Wang, H. M. Zhou, J. He, M. Zhong, X. Z. Lan, Y. S. Zhou, Z. Q. Wang, J. Li, A. Seifitokaldani, C. T. Dinh, H. Y. Liang, C. Q. Zou, D. L. Zhang, Y. Yang, T. S. Chan, Y. Han, L. Cavallo, T. K. Sham, B. J. Hwang and E. H. Sargent, *Joule*, 2019, **3**, 1703-1718.
54. H. C. Zhang, X. X. Chang, J. G. G. Chen, W. A. Goddard, B. J. Xu, M. J. Cheng and Q. Lu, *Nat. Commun.*, 2019, **10**, 3340.